High-Temperature Deformation Behavior of Coarse- and Fine-Grained $MoSi_2$ with Different Silica Contents

R. MITRA, N. ESWARA PRASAD, SWEETY KUMARI, and A. VENUGOPAL RAO

The elevated-temperature deformation behavior of polycrystalline molybdenum disilicide ($MoSi_2$), in the range of 1000 °C to 1350 °C at the strain rates of 10^{-3}, 5×10^{-4}, or 10^{-4} s^{-1}, has been studied. The yield strength, post-yield flow behavior comprising strain hardening and serrations, as well as some of the deformation microstructures of reaction-hot-pressed (RHP) $MoSi_2$ samples, processed by hot pressing an elemental Mo + Si powder mixture and having a grain size of 5 μm and oxygen content of 0.06 wt pct, have been compared with those of samples prepared by hot pressing of commercial-grade Starck $MoSi_2$ powder, with a grain size of 27 μm and oxygen content of 0.89 wt pct. While the fine-grained RHP $MoSi_2$ samples have shown higher yield strength at relatively lower temperatures and higher strain rates, the coarse-grained Starck $MoSi_2$ has a higher yield at decreasing strain rates and higher temperatures. The work-hardening or softening characteristics are dependent on grain size, temperature, and strain rate. Enhanced dislocation activity and dynamic recovery, accomplished by arrangement of dislocations in low-angle boundaries, characterize the deformation behavior of fine-grained RHP $MoSi_2$ at a temperature of 1200 °C and above and are responsible for increased uniform plastic strain with increasing temperature. The silica content appears to be less effective in degrading the high-temperature yield strength if the grain size is coarse, but leads to plastic-flow localization and strain softening in Starck $MoSi_2$. Serrated plastic flow has also been observed in a large number of samples, mostly when deformed at specific combinations of strain rates and temperatures.

I. INTRODUCTION

Molybdenum disilicide ($MoSi_2$) has evoked a great deal of interest in the research community for high-temperature structural applications above 1000 °C, because of its high melting point of as high as 2020 °C, outstanding oxidation resistance up to 1700 °C, and brittle-to-ductile transition temperature (BDTT) in the range of 1000 °C to 1300 °C. The added advantages over other oxidation-resistant ceramics are its limited ductility around and above 1000 °C to 1200 °C and its electrical conductivity. For its outstanding oxidation resistance and adequate electrical resistivity, it has been used in the heating element "superkanthal" (Bysakh and Company, Kolkata, India) in high-temperature air furnaces. In recent years, applications have been proposed or are being attempted in hot-end components of aerospace gas turbines, diesel engine glow plugs, and molten-metal lances.[1]

Having being projected as a material for high-temperature structural applications, the thrust of research on $MoSi_2$ has been on improving the high-temperature mechanical properties[2-12] and establishing a comprehensive understanding of deformation mechanisms.[11-25] Single-crystal $MoSi_2$ has been found to plastically deform even at room temperature[13] in relatively "soft" orientations away from [001], such as [110], [201], or [0 15 1], while polycrystalline $MoSi_2$ cannot deform without cracking until 1000 °C, as only four independent slip systems have been found to be active at or below 1000 °C.[14] The five most active slip systems reported by Ito *et al.*[15] are {013}⟨331⟩, {110}⟨111⟩, {011}⟨100⟩, {010}⟨100⟩, and {023}⟨100⟩. Maloy *et al.*[14] have reported that {011}⟨100⟩ slip is active at all temperatures, is the primary slip system while {110} 1/2⟨111⟩ comprises the secondary slip system, and is activated at 600 °C. The critically resolved shear stress (CRSS) of the slip system {013} 1/2⟨331⟩ is very much dependent on crystal orientation and is very high for crystals with a stress axis near the [001] orientation at temperatures lower than 1300 °C.[13] The strong orientation dependence of the CRSS of the {013} 1/2⟨331⟩ slip system could be used to explain the high BDTT of polycrystalline $MoSi_2$. But, there are other factors affecting the onset of plastic deformation. From the measurement of outer fiber strain in four-point bend specimens,[2] the BDTT in $MoSi_2$ has been reported as 1300 °C, irrespective of SiO_2 content. Some articles[3,4] have however, reported 1000 °C to 1200 °C as the BDTT in $MoSi_2$. Carter *et al.*[3] have observed the occurrence of plastic deformation during a four-point bend test at 1200 °C. Srinivasan *et al.*[4] have, however, reported from the comparison of mechanically alloyed samples containing 0.19 and 0.09 wt pct O and identical grain sizes that the sample with higher oxygen content has shown significant plastic deformation in bending at 1200 °C, while the sample with lower oxygen content has not shown any. The sample with high oxygen content has shown a continuous layer of SiO_2 at the grain boundary, while a sample with lower SiO_2 content has shown only discrete SiO_2 particles. The previous results imply that plasticity in $MoSi_2$ with a high impurity or SiO_2 content is probably due to grain-boundary sliding, facilitated by viscous flow of a glassy phase. It has been argued[4] that the viscous flow of glassy phase releases

R. MITRA, formerly Scientist "E," Defence Metallurgical Research Laboratory, is Assistant Professor, Department of Metallurgical and Materials Engineering, Indian Institute of Technology, Kharagpur–721 302, West Bengal, India. Contact e-mail: rahul_mitra2001@yahoo.com or rahul@metal.iitkgp.ernet.in N. ESWARA PRASAD, Scientist "E," SWEETY KUMARI, Scientist "B," and A. VENUGOPAL RAO, Scientist "D," are with the Defence Metallurgical Research Laboratory, Hyderabad–500 058, India.

Manuscript submitted April 25, 2002.

the stress concentration at the grain boundaries. In an earlier publication, Mitra *et al.*[6] have reported on the high-temperature hardness tests on a $MoSi_2$-SiC composite with 0.24 wt pct O and with a matrix grain size of 18 μm, that cracking at corners of indentations could be observed from room temperature to 1000 °C, but not at 1100 °C. Also, Chang *et al.*[7] have reported extensive microcracking in the $MoSi_2$ samples tested in compression at 1000 °C or below with a strain rate of 10^{-4} s^{-1}, whereas significant dislocation plasticity was observed in the samples tested at 1100 °C or above. Limited microcracking was observed in samples tested at 1100 °C, which was not found in the samples tested at a higher temperature. It should be noted that tests conducted by Aikin[2] and Srinivasan *et al.*[4] were in bending, while those of Chang *et al.*[7] were in compression. Bend tests involve the application of both tensile and compressive loading, and failure initiates in the area experiencing maximum tensile stress. On the other hand, compressive loading inhibits failure by void growth and linkage, while plastic deformation takes place as the yield stress is reached. The BDTT has also been lowered by generation of dislocations in the $MoSi_2$ grains in $MoSi_2$-ZrO_2[26,27] and $MoSi_2$-TiC composites[7,27] during processing, where particle-matrix interfaces have acted as sources of dislocations. At 1200 °C and above, more than five independent slip systems,[11] {013} ½⟨331⟩, {013}⟨100⟩, {010}⟨100⟩, {001}⟨110⟩, {011}⟨100⟩, and {110} ½⟨111⟩, are activated, which render the $MoSi_2$ completely deformable. There are a significant number of publications on the dislocation structure of single[13,15,18,21-25] and polycrystalline[14,16,17,28] $MoSi_2$ deformed at different temperatures and strain rates, chiefly at 10^{-4} s^{-1} or slower.

The high-temperature hardness, yield strength, and creep resistance of $MoSi_2$ depend on the grain sizes and silica (SiO_2) content, as has been pointed out.[2,4-6,8] The reduction of strength due to smaller grain size or high SiO_2 content, as found in the high-temperature compression or bend tests[2] and creep tests,[29,30,31] has been reported widely in the past. However, it is also a well-known fact that below the equicohesive temperature, grain boundaries are stronger than the grain interior, whereas at a higher temperature, grain boundaries are weaker than the grain interior. Besides temperature, the role of grain boundaries in deformation also depends on the strain rates, impurities, and SiO_2 content. One of the startling properties of $MoSi_2$ has been the strong dependence of creep behavior[31] on grain size, even in the dislocation-creep regime. Due to the fact that $MoSi_2$ is a stoichiometric line compound with covalent Mo-Si bonds, Mo and Si atoms are constrained to diffuse in their respective planes. As a result, the grain-boundary diffusion rate is much higher than the lattice diffusion, which contributes to the process of recovery by dislocation climb. Probably, the high rate of grain-boundary diffusion explains why the grain-size exponent in the dislocation-creep regime has been determined to be equal to 4.3, which is almost similar to that measured in the diffusion-creep regime in $MoSi_2$ and is larger than the grain-size exponents of 2 or 3 in the case of the Nabarro–Herring or Coble creep regimes, respectively.

In this investigation, $MoSi_2$ samples prepared by *in-situ* processing or by conventional vacuum hot pressing and having either a fine or coarse grain size and different SiO_2 contents have been tested in compression at initial strain rates between 10^{-3} and 10^{-4} s^{-1} at temperatures between 1000 °C (0.55 T_m) and 1350 °C (0.71 T_m), with emphasis on understanding the effect of grain size and SiO_2 content, strain rate, and temperature on yielding and deformation behavior. As the existing literature on polycrystalline $MoSi_2$ contains data on deformation mechanisms, structure, or properties at strain rates of 10^{-4} s^{-1} or slower, with not much emphasis on flow-curve characteristics, this work has attempted to highlight the mechanical properties, flow behavior, and deformation substructure at strain rates higher than those reported in the past. The room-temperature mechanical properties of the $MoSi_2$ samples studied in this investigation have been discussed elsewhere.[6]

II. EXPERIMENTAL

A. *Processing*

The $MoSi_2$ was processed in the form of discs of 75 mm in diameter and 6 mm in height by reaction hot pressing or conventional vacuum hot pressing. In the reaction-hot-pressing process, intimately mixed Mo and Si powders were hot pressed at 1500 °C in vacuum (10^{-4} Pa), using 26 MPa pressure. Prior to hot pressing, vacuum degassing was performed at 800 °C for 4 hours. The Mo powder was obtained from Non-Ferrous Technology Development Corporation (Hyderabad, India) and had a particle size of 3 μm, while the Si powder was obtained from Johnson Matthey, Inc. (New York, NY) and had a particle size of 20 μm. The details of the reaction-hot-pressing process, with a discussion of the thermodynamics and kinetics, have been reported in an earlier publication.[6] In conventional vacuum hot pressing, $MoSi_2$ powder from H.C. Starck, (Selb, Germany) with a particle size of 5.5 μm was used. The Starck $MoSi_2$ was hot pressed at 1700 °C in vacuum, also using 26 MPa pressure, after vacuum degassing at 1000 °C for 2 hours. The chemical composition of the Mo, Si, and $MoSi_2$ powders used is shown in Table I.

B. *Characterization*

A method of instrumental analysis using an inert-gas carrier technique has been used for measuring the oxygen content. Microstructures have been studied using polarized-light optical microscopy, X-ray diffraction, scanning electron microscopy, and electron-probe microanalysis. Samples were prepared by argon ion milling and were examined on at Hitachi H8100 (Tokyo, Japan) transmission electron microscope (TEM) or HF2000 high-resolution TEM (HRTEM) at an accelerating voltage of 200 kV.

Table I. Chemical Composition of Impurities in Mo, Si, and Starck $MoSi_2$ Powders

Powder (Source)	Impurity Content (Wt Pct)
Mo Powder (NFTDC)	W ≈ 0.62, Fe ≈ 0.018, C ≈ 0.052, O ≈ 1.3
Si Powder (Johnson Matthey, Inc.)	Fe ≈ 0.21, Mg ≈ 0.01, C ≈ 0.021, O ≈ 0.23
$MoSi_2$ (H.C. Starck)	Fe ≈ 0.11, Mn ≈ 0.036, C ≈ 0.08, O ≈ 1.0, N ≈ 0.032

The samples of 3 mm in diameter and 6 mm in height were fabricated using electrodischarge machining. Compression tests were carried out between 1000 °C and 1350 °C in air on a servohydraulic DARTEC (Herefordshire, U.K.) machine at initial strain rate of 10^{-3} s^{-1} or on an INSTRON (Canton, MA) 8801 machine at the initial strain rates of 5×10^{-4} and 10^{-4} s^{-1}. Both in the INSTRON and DARTEC machines, tests were repeated and the results were found to be reproducible, with the yield stress not differing by more than 3 MPa. Also, there has been an excellent agreement between the yield strengths obtained from the DARTEC and INSTRON 8801 machines, when repeat tests were carried out under similar conditions of temperature and strain rate.

Both the DARTEC and INSTRON machines are equipped with rigid alumina push rods and SiC platens. During testing, the thermocouple was kept close to the sample inside the furnace, which was equipped with a superkanthal heating element. For calculating the plastic strains, crosshead displacements, with the elastic component deducted, have been used. In the DARTEC machine, the tests were carried out at constant strain rate. For each test using the DARTEC machine, eight data points were recorded per second. The samples were deformed to either 20 to 30 pct plastic strain or stopped soon after the rate of drop in load became sharp. Using the INSTRON 8801 machine, tests were carried out at a constant crosshead velocity and stopped after 6 to 10 pct plastic strain. For each test using the INSTRON machine, two, five, or ten data points per second were recorded, with higher data acquisition rates being employed at higher strain rates. As the serrations in some of the flow curves were very sharp, the program would take it as a failure and stop the test. As a result, most of the tests carried out on the INSTRON machine were with a low data input per second.

Some of the deformed samples were sectioned at 45 deg to the vertical axis, and thin slices were cut, polished, and prepared for TEM studies. The TEM specimens were prepared by mechanical polishing, followed by argon ion milling. Some of the vertically sectioned samples were cold mounted and polished for metallographic examination.

III. RESULTS

A. *Microstructure*

Using Archemedes' principle, the densities of reaction-hot-pressed (RHP) $MoSi_2$ and Starck $MoSi_2$ have been found to be 95 and 99 pct of the theoretical density, respectively. Figures 1(a) and (b) show the polarized-light optical micrographs of RHP $MoSi_2$ and Starck $MoSi_2$, respectively. The average grain size of RHP and Starck $MoSi_2$, estimated using the linear-intercept method, are 5 and 27 μm, respectively. In RHP $MoSi_2$, a correlation has been found between Mo particle size and the grain size of the RHP $MoSi_2$. Mo particle sizes of 3 and 15.5 μm have resulted in the formation of $MoSi_2$ with grain sizes of 5 and 16 μm, respectively. It has been suggested in an earlier publication[6] that Si atoms diffuse and react with Mo, forming $MoSi_2$ at the site of pre-existing Mo particles, while the reaction proceeds from the surface to interior. The $MoSi_2$ grains grow, approximately, up to the prior-particle boundaries. Probably, the oxides present at the prior-particle boundaries are either reduced or vaporize in vacuum or in the slightly reducing environment present. No correlation has been found between the Si particle size and $MoSi_2$ grain size, as Si is in a molten state at 1500 °C. The grain size of Starck $MoSi_2$ shows a wider variation between 15 and 40 μm compared to that of RHP $MoSi_2$, because of grain growth during hot pressing at the higher temperature (1700 °C).

The oxygen contents of RHP and Starck $MoSi_2$ have been found to be 0.06 and 0.89 wt pct respectively. The oxygen in $MoSi_2$ is found in the form of SiO_2 particles. The microstructure of Starck $MoSi_2$ (Figure 1(b)) shows globular SiO_2 particles, which appear bright in polarized light. The SiO_2 particles are distributed both inside the grain as well as at the grain boundaries of Starck $MoSi_2$. On the other hand, such SiO_2 particles have not been observed in the RHP $MoSi_2$ as frequently as in Starck $MoSi_2$, because of its lower oxygen content because and the grain boundaries are free of SiO_2 particles (Figure 1(a)). The microstructure and the reasons for differences in density, oxygen content, and grain size, and the role of

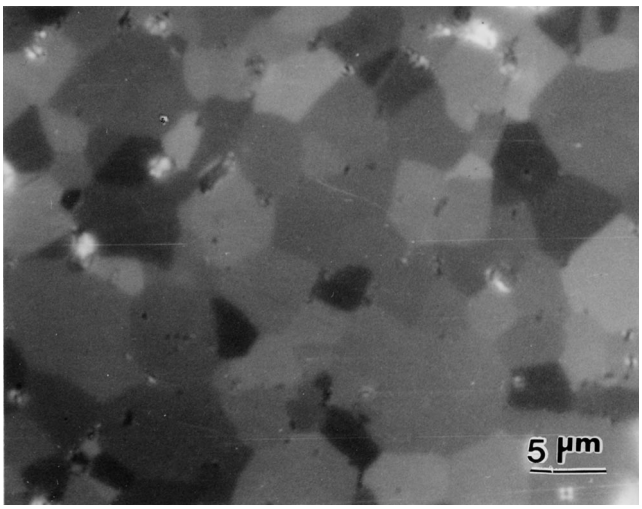

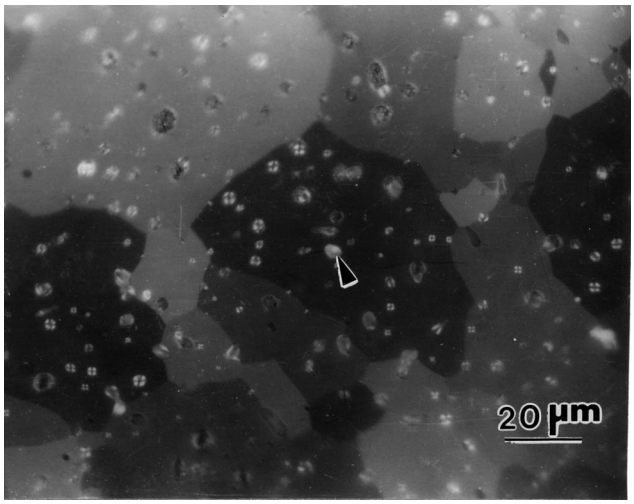

processing methods used, have been discussed in detail in an earlier publication.[6]

B. *Mechanical Behavior*

1. *Yield stress*

The plots showing the variation with temperature of the compressive yield stress corresponding to 0.2 pct plastic strain, in the engineering stress-strain curves of RHP $MoSi_2$ and Starck $MoSi_2$, which were tested at the strain rates of 10^{-4}, 5×10^{-4}, and 10^{-3} s^{-1} in the range of 1000 °C to 1350 °C, are shown in Figure 2. The yield strength of both RHP and Starck $MoSi_2$ decreases with increasing temperature at all three strain rates. Figure 2 also shows that the yield strength of fine-grained RHP $MoSi_2$ is more strongly dependent on temperature, compared to Starck $MoSi_2$. Tables II and III show the yield stress (σ_y) and maximum stress (σ_{max}) obtained in the flow curves of RHP and Starck $MoSi_2$, respectively. Tables II and III also show that the ratio σ_{max}/σ_y of RHP $MoSi_2$ increases with increasing temperature for a specific strain rate. On the other hand, the σ_{max}/σ_y ratio of Starck $MoSi_2$ decreases with increasing temperature for a specific strain rate. The true plastic strain at the maximum stress of each flow curve ($\varepsilon_{p,m}$) is also shown in Tables II and III. The trend followed by $\varepsilon_{p,m}$ in the case of RHP (Table II) and Starck (Table III) $MoSi_2$ is similar to that of σ_{max}/σ_y. These observations are discussed in detail in Section IV–B–2. The equipment used (INSTRON or DARTEC) is shown in parentheses next to the temperature in Tables II and III. In the cases of repeat tests in both machines, INSTRON results have been shown for comparison.

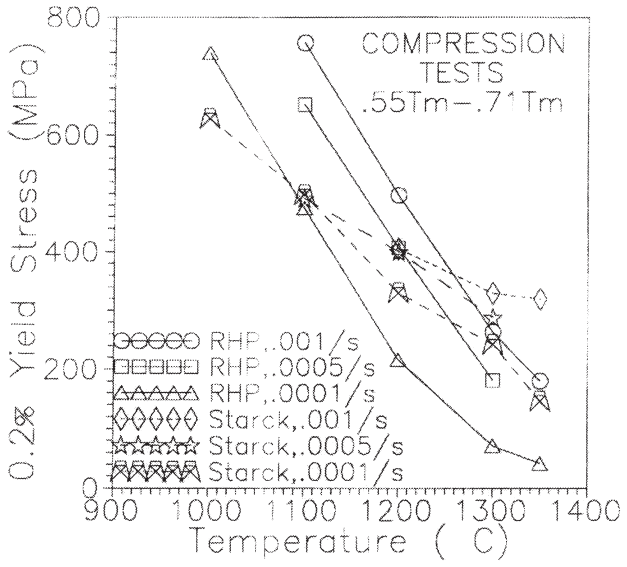

Fig. 2—Plots showing variation of 0.2 pct compressive yield stress of RHP $MoSi_2$ (solid lines) and Strack $MoSi_2$ (dashed lines) at strain rates of 10^{-4} s^{-1}, 5×10^{-4} s^{-1}, and 10^{-3} s^{-1} with temperature between 1000 °C (0.55 T_m) and 1350 °C (0.71 T_m).

2. *Plastic flow*

In addition to the yield stress, the plastic-flow behavior is also a function of the grain size, strain rate, and temperature. Figures 3(a) through (c) show the load-displacement or engineering stress-strain curves of RHP $MoSi_2$, corresponding to deformation in the temperature range of 1000 °C to 1350 °C at strain rates of 10^{-4}, 5×10^{-4}, and 10^{-3} s^{-1}, respectively. The load-displacement or engineering stress-strain curves of Starck $MoSi_2$ in the temperature range of 1000 °C to 1350 °C and corresponding to the strain rates of 10^{-4}, 5×10^{-4}, and 10^{-3} s^{-1} are shown in Figures 4(a) through (c), respectively. The true plastic strain corresponding to the maximum stress in the flow curve also varies in RHP (Table II) and Starck (Table III) $MoSi_2$ with the temperature and strain rate of the compression tests. In case of RHP $MoSi_2$, $\varepsilon_{p,m}$ increases sharply with increasing temperature (Table II), such that on testing at a strain rate of 10^{-4} s^{-1} and at the temperature of 1350 °C, $\varepsilon_{p,m}$ exceeds 6 pct. In the case of Starck $MoSi_2$, $\varepsilon_{p,m}$ decreases with increasing temperature.

The rate of strain hardening ($d\sigma/d\varepsilon$) of RHP and Starck $MoSi_2$, corresponding to the strain rate of 5×10^{-4} s^{-1}, is plotted with respect to true plastic strain in Figures 5(a) and (b), respectively. The mean strain-hardening rates (SHRs) corresponding to different flow curves of RHP and Starck $MoSi_2$ have been normalized by the shear modulus (G) corrected for temperature[33] and are shown in Tables II and III. The mean value has been calculated by taking the average of the SHR at a true plastic strain close to 0.1 pct and that

Table II. Values of σ_y, σ_{max}, σ_{max}/σ_y, Mean SHR Normalized by Shear modulus, G (Corrected for Temperature), Strain Hardening Exponents, n and n_1, Strain Softening Parameter γ_s, and True Plastic Strain at Maximum Stress $\varepsilon_{p,m}$ from the Flow Curves* of RHP $MoSi_2$ (Mean Grain Size = 5 μm, and Oxygen Content = 0.06 wt. pct.)

Strain Rate(s^{-1})	T (°C) and Machine	σ_y (MPa)	σ_{max} (MPa)	σ_{max}/σ_y	SHR/G (X 10^2)	n	n_1	γ_s	$\varepsilon_{p,m}$
10^{-3}	1100 (D)	757	758	1.001	8.0	0.44	—	6.1	0.0025
10^{-3}	1200 (D)	497	594	1.194	0.71	0.14	—	—	0.0095
10^{-3}	1300 (D)	263	313	1.190	0.70	0.19	—	—	0.018
10^{-3}	1350 (I)	180	217	1.205	1.26	0.29	0.84	—	0.0253
5×10^{-4}	1100 (I)	626	652	1.042	5.55	0.40	0.57	10.1	0.0055
5×10^{-4}	1200 (I)	407	440	1.081	2.74	0.28	0.42	—	0.010
5×10^{-4}	1300 (I)	181	214	1.182	1.01	0.20	0.35	—	0.0219
10^{-4}	1000 (I)	740	747	1.009	1.39	0.07	0.08	23.3	0.0047
10^{-4}	1100 (I)	475	517	1.088	4.84	0.31	0.50	8.7	0.0044
10^{-4}	1200 (I)	216	244	1.131	1.38	0.22	0.36	—	0.0132
10^{-4}	1300 (I)	72	94	1.315	0.31	0.183	0.32	—	0.0492
10^{-4}	1350 (I)	42	—	—	0.28	0.209	0.56	—	>0.06

*The equipment used, INSTRON or DARTEC, is shown in parentheses next to the temperature as (I) or (D), respectively.

Table III. Values of σ_y, σ_{max}, σ_{max}/σ_y, Mean SHR Normalized by Shear Modulus, G (Corrected for Temperature), Strain Hardening Exponents, n and n_1, Strain Softening Parameter γ_s, and True Plastic Strain at Maximum Stress $\varepsilon_{p,m}$ from the Flow Curves* of Starck $MoSi_2$ (Mean Grain Size = 27 μm, and Oxygen Content = 0.89 wt pct)

Strain rate (s^{-1})	T (°C) Machine	σ_y (MPa)	σ_{max} (MPa)	σ_{max}/σ_y	SHR/G X 10^2	n	n_1	γ_s	$\varepsilon_{p,m}$
10^{-3}	1200 (I)	405	452	1.116	2.32	0.38	0.48	—	0.0161
						0.13	0.17		
10^{-3}	1300 (D)	329	333	1.011	5.40	0.38	—	—	0.0042
10^{-3}	1350 (I)	322	328	1.018	1.80	0.18	0.33	12	0.0038
5×10^{-4}	1100 (I)	492	557	1.132	3.51	0.27	0.42	—	0.0126
5×10^{-4}	1200 (I)	407	431	1.059	2.0	0.22	0.40	—	0.0096
5×10^{-4}	1300 (I)	285	289	1.014	0.84	0.10	0.12	5.6	0.0042
10^{-4}	1000 (I)	628	672	1.07	1.38	0.13	0.27	—	0.0236
						0.04	0.15		
10^{-4}	1100 (I)	498	555	1.114	2.0	0.25	0.61	—	0.0251
						0.05	0.18		
10^{-4}	1200 (I)	330	358	1.086	1.35	0.14	0.44	—	0.0119
10^{-4}	1300 (I)	242	245	1.014	0.73	0.08	0.12	10.2	0.0047
10^{-4}	1350 (I)	146	147	1.007	1.92	0.35	0.79	6.8	0.0027

*The equipment used, INSTRON or DARTEC, is shown in parentheses next to temperature as (I) or (D), respectively.

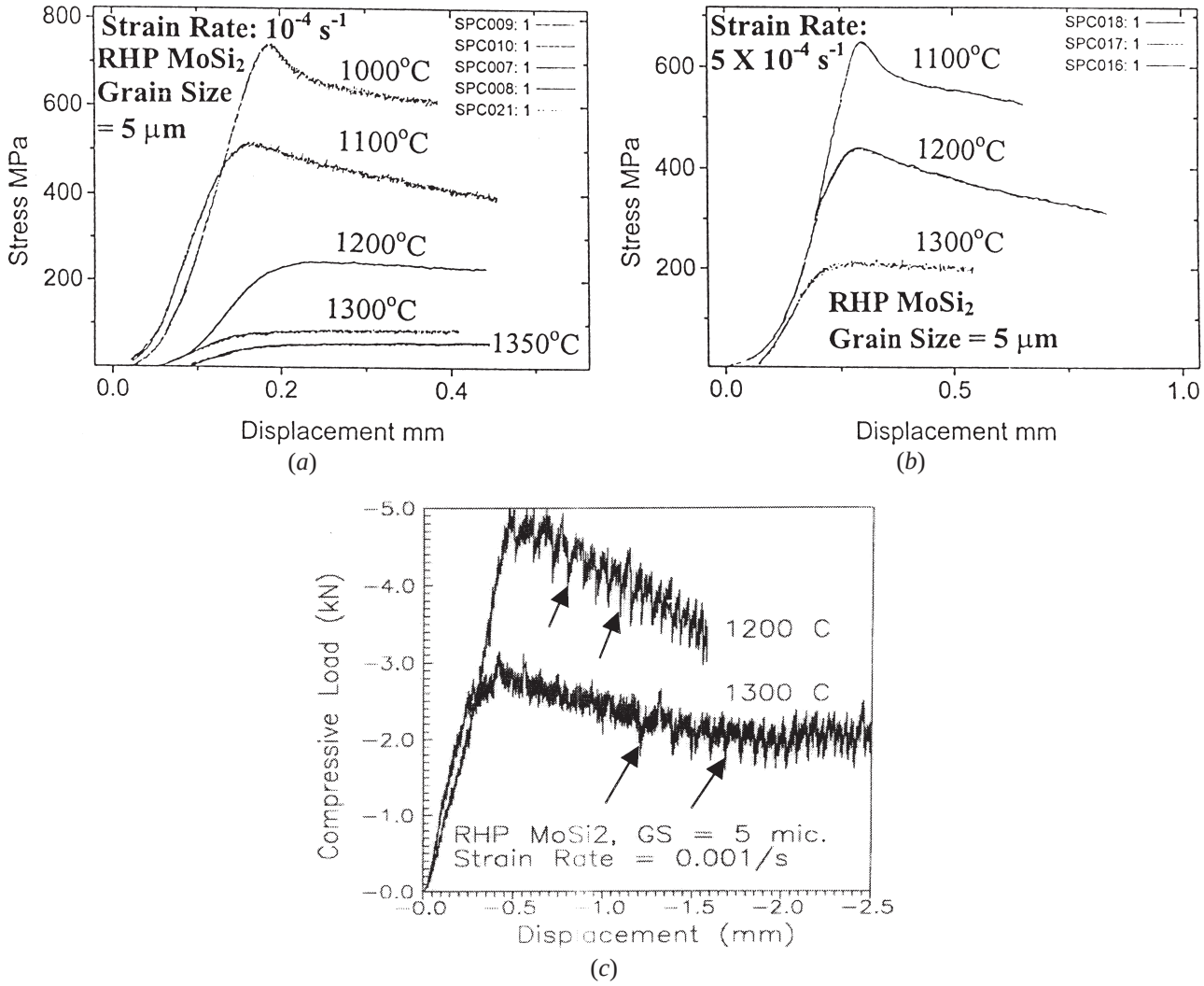

Fig. 3—Load displacement or engineering stress displacement curves of RHP $MoSi_2$, corresponding to strain rates of (*a*) 10^{-4} s^{-1}, (*b*) 5×10^{-4} s^{-1}, and (*c*) 10^{-3} s^{-1}. Serrations are shown with an arrow in Fig. 3(c).

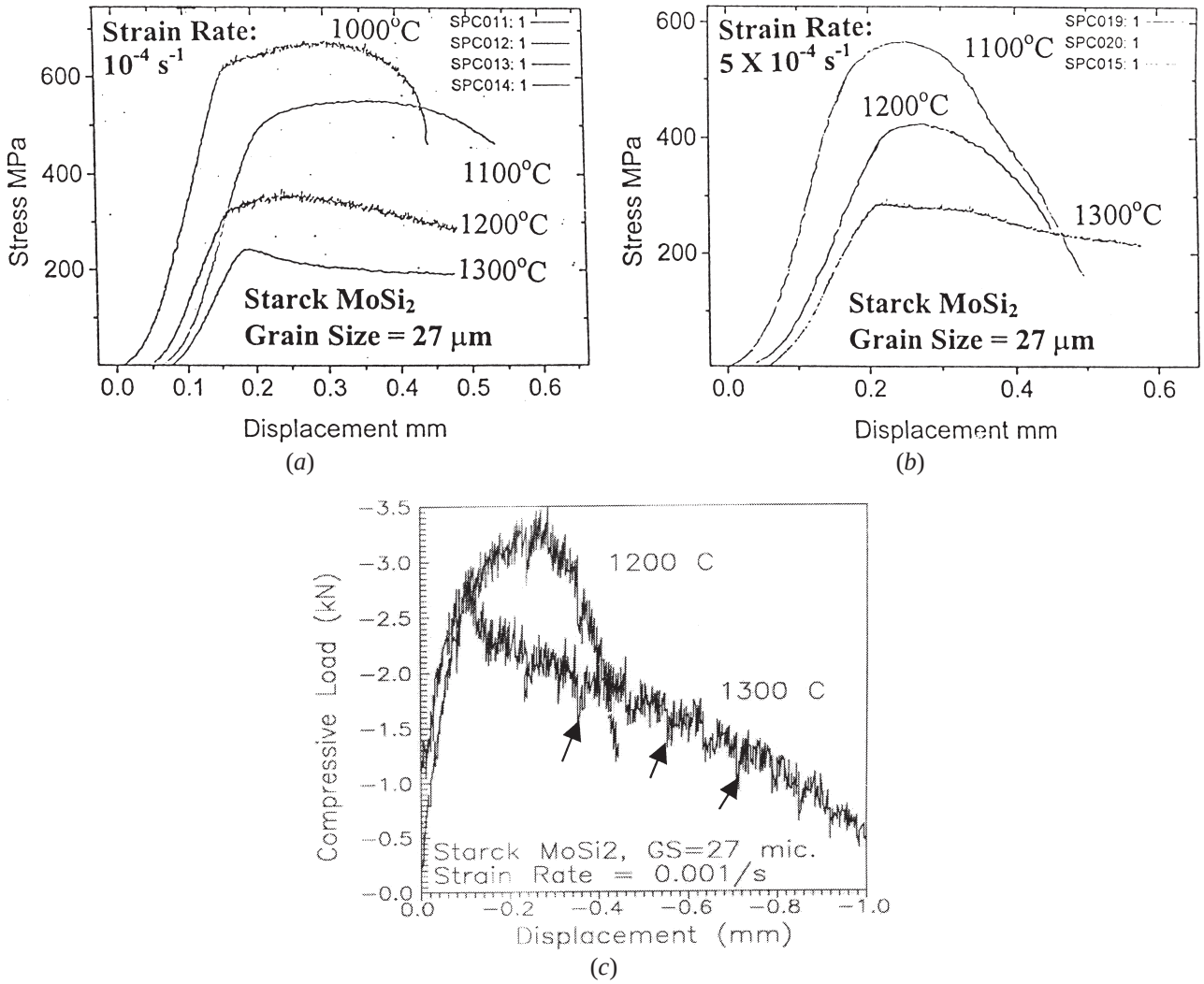

Fig. 4—Load displacement or engineering stress displacement curves of Strack $MoSi_2$, corresponding to strain rates of (*a*) 10^{-4} s^{-1}, (*b*) 5×10^{-4} s^{-1}, and (*c*) 10^{-3} s^{-1}. Serrations are shown with an arrow in Fig. 4(c).

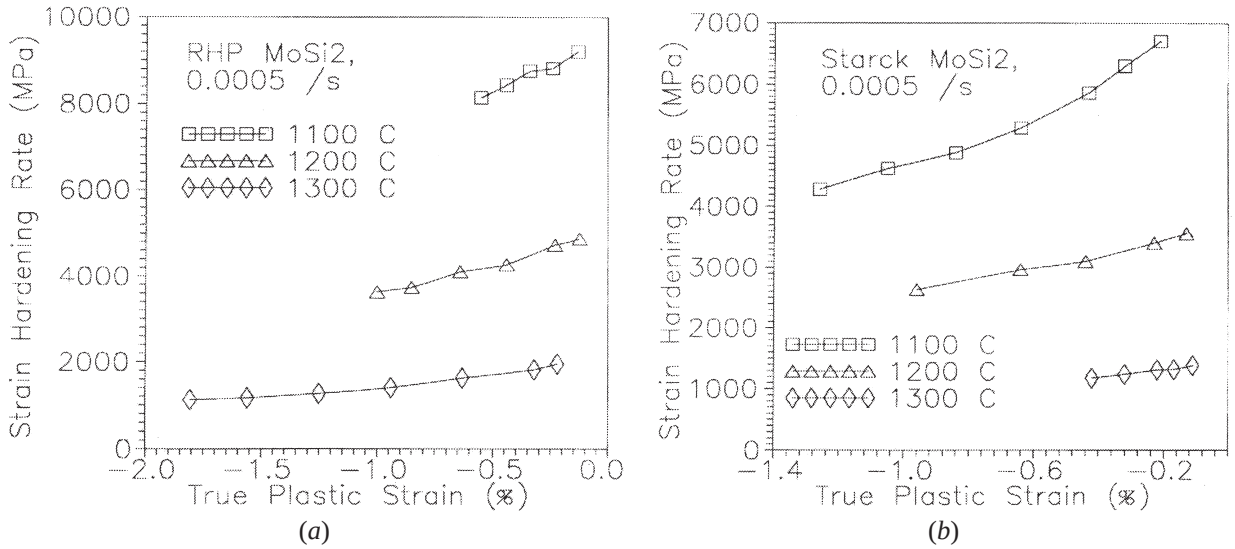

Fig. 5—Variation of strain hardening, $d\sigma/d\varepsilon$, with true plastic strain, ε_p, of (*a*) RHP $MoSi_2$ and (*b*) Starck $MoSi_2$, tested at strain rates of 5×10^{-4} s^{-1}.

approaching $\varepsilon_{p,m}$. The other strain-hardening and softening parameters, which are shown in Tables II and III, are explained and discussed in Section IV–B.

Serrations have been observed in the flow curves corresponding to the tests at strain rates of 10^{-3} s^{-1} on RHP $MoSi_2$ at 1100 °C to 1300 °C and on Starck $MoSi_2$ at 1300 °C. Serrations have been also found in some of the flow curves, corresponding to the tests carried out on the INSTRON machine at 10^{-4} or 5×10^{-4} s^{-1}. However, the tests carried out on the DARTEC machine at the strain rate of 10^{-3} s^{-1} have shown serrations more vividly, which could be either due to the fact that more data points per second could be recorded, or the characteristic strain rate for maximization in the serrated flow behavior could be around 10^{-3} s^{-1}. The fact that serrations are easily distinguishable in the flow curves corresponding to tests using the DARTEC machine may be established from the comparison of the flow curve corresponding to the test on Starck $MoSi_2$ at 1300 °C with a strain rate of 5×10^{-4} s^{-1} (Figure 6) with that carried out on the INSTRON machine (Figure 4(b)). Further discussion is reported in Section IV–B.

3. *Deformation microstructure*

Figures 7(a) and (b) are polarized-light optical micrographs of RHP and Starck $MoSi_2$, respectively, deformed at 1300 °C (0.68 T_m) with a strain rate of 10^{-3} s^{-1}. The RHP $MoSi_2$ has not shown any evidence of grain growth or microcracking, even after a true plastic strain of 34.3 pct. On the other hand, Starck $MoSi_2$ has shown transgranular and intergranular cracks after a plastic strain of even 10 pct. The corresponding flow curve (Figure 3(c)) of RHP $MoSi_2$ has shown no evidence of softening, while that of Starck $MoSi_2$ (Figure 4(c)) has shown softening characteristics. Figure 8 shows the area with flow localization and cracking from the vertical cross section of RHP $MoSi_2$ deformed in compression to a plastic strain of 51 pct (measured from specimen dimensions before and after the test) at 1200 °C with a strain rate of 5×10^{-4} s^{-1}. The rest of the sample has not shown any evidence of cracking or cavitation. The observation of a localized cracking pattern in Figure 8 agrees with the softening characteristic of the flow curve, corresponding to deformation at 1200 °C with a strain rate of 5×10^{-4} s^{-1}.

In the RHP $MoSi_2$ of 5 μm grain size, recovery sets in by the formation of low-angle boundaries (Figures 9(a) through (c)) assisted by climb, even when deformed at 1200 °C using a strain rate of 10^{-3} s^{-1}. In RHP $MoSi_2$, geometrically necessary dislocations form low-angle boundaries by climb even in the samples deformed at 1200 °C and a strain rate of 10^{-3} s^{-1} (Figures 9(a) and (b)), which have been observed previously[17] in coarse-grained samples tested at 1400 °C and a strain rate of 10^{-5} s^{-1}. Figures 9(a) and (b) and bright- and dark-field TEM micrographs, respectively, of a $MoSi_2$ grain, showing at least four low-angle boundaries (arrows in Figure 9(b)). The dislocations observed in Figures 9(a) and (b) have a Burgers vector of ⟨100⟩ or ½ ⟨111⟩. Figures 9(a) through (c) also show that lattice dislocations interact with the low-angle grain-boundary dislocations and are suggested to be in the process of either joining the boundary or being emitted from it at the ledges. It is worth noting that grain-boundary ledges have been suggested and shown to be the sources of dislocations.[34,35,36]

However, low-angle boundaries are not observed in all the grains of samples tested at 1200 °C with a strain rate of

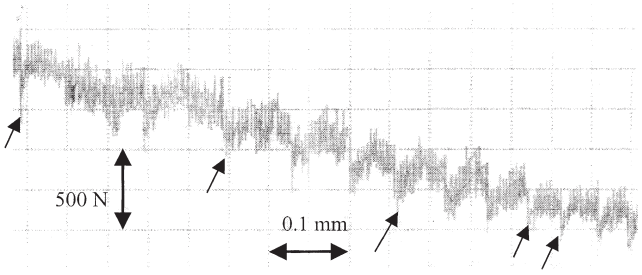

Fig. 6—Serrated plastic flow observed in Starck $MoSi_2$, when tested at 1300 °C and strain rate of 5×10^{-4} s^{-1} (serrations arrowed) on DARTEC.

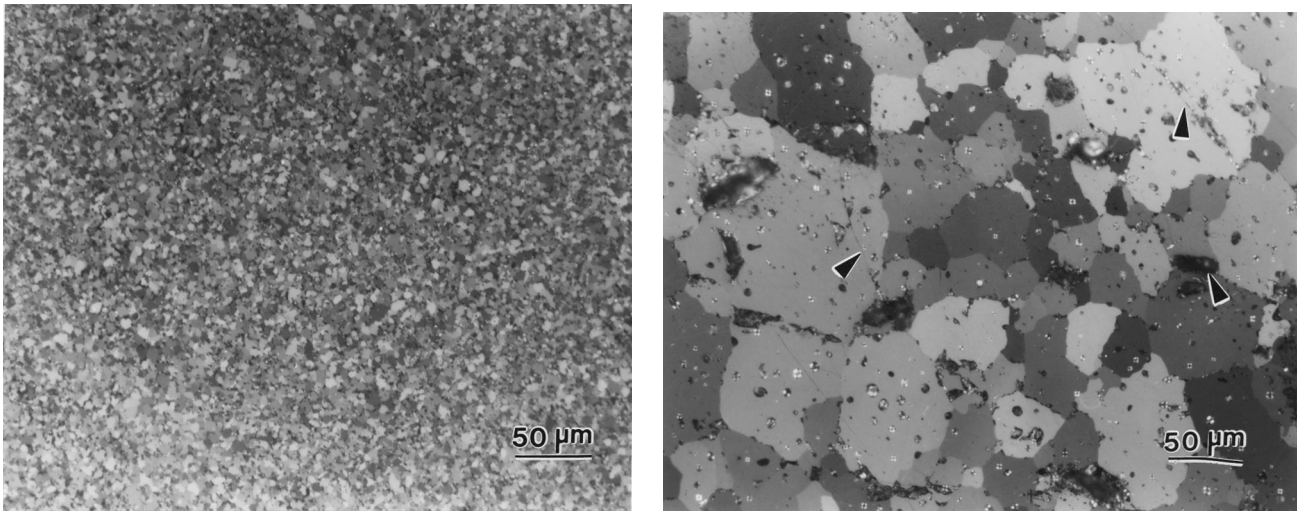

(*a*) (*b*)

Fig. 7—Polarized light optical micrographs of (*a*) RHP and (*b*) Strack $MoSi_2$ deformed at 1300 °C (0.68 T_m), using a strain rate of 10^{-3} s^{-1}. Transgranular and intergranular cracks in Starck $MoSi_2$ are shown with arrows.

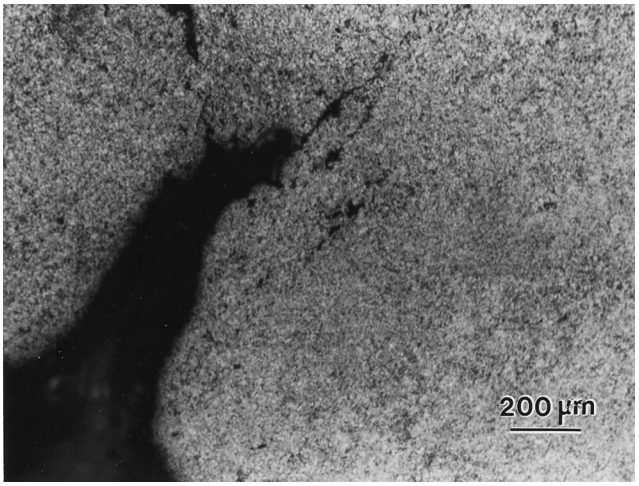

Fig. 8—Polarized light optical micrograph from a vertical cross section of RHP $MoSi_2$, deformed to a plastic strain of 51pct with a strain rate of 5×10^{-4} s^{-1} at 1200 °C, showing the region with a crack.

10^{-3} s^{-1}. Evidence of the formation of dislocation nodes was observed within some grains (Figure 10(a)). The Burgers vectors of dislocations, shown in bright-field (Figure 10(a)) and dark-field (Figures 10(b) and (c)) micrographs, have been determined using the "g · b" analysis. The dark-field images were recorded at close to two-beam conditions using the diffraction vectors **g = [0$\bar{1}$3], [211], [21$\bar{3}$], [112],** and **[$\bar{2}$0$\bar{4}$].**

The dislocation reactions are suggested to be

$$\text{D1: } [\bar{1}00] + [010] \rightarrow [\bar{1}10]$$

$$\text{D2: } \tfrac{1}{2}[111] + [\bar{1}00] \rightarrow \tfrac{1}{2}[\bar{1}11]$$

$$\text{D3: } \tfrac{1}{2}[\bar{3}31] \rightarrow \tfrac{1}{2}[\bar{1}11] + [\bar{1}10]$$

The dislocation-node structure found in the RHP $MoSi_2$ sample deformed at 1200 °C with a strain rate of 10^{-3} s^{-1} has also been reported in samples deformed at lower temperatures and strain rates of 10^{-4} s^{-1} or less.[7,14,16,20]

Using TEM and HRTEM studies of deformed RHP $MoSi_2$, no evidence of grain-boundary amorphous film formation or cracking could be observed. Figure 11 shows an HRTEM image of a grain boundary in RHP $MoSi_2$, which has been deformed at 1200 °C on the DARTEC machine, using a strain rate of 10^{-3} s^{-1}, to a true plastic strain of 18.7 pct. On the contrary, amorphous film of SiO_2 has been observed along with intergranular cracks in Starck $MoSi_2$ (Figures 12(a) and (b)) deformed at 1300 °C with a strain rate of 10^{-3} s^{-1}. The sample of Starck $MoSi_2$ deformed at 1200 °C with a strain rate of 10^{-3} s^{-1} cracked during testing. During high-temperature deformation, the SiO_2 particles, which happen to be globular in shape to begin with (Figure 1(b)), soften and flow in a viscous manner, ending up as an intergranular amorphous film. The meniscus at the tip of the film shows that SiO_2 wets the $MoSi_2$ grain boundaries at high temperature and on application of stress. The amorphous intergranular film is stretched due to sliding between the deforming grains and eventually cracks, as shown in Figure 12(a). The $MoSi_2$ grains have normally shown dislocation pileups and nodes (Figure 12(b)), but low-angle boundary formation could also be seen in isolated areas. Figure 12(c) shows an electron diffraction pattern with a diffuse halo contributed by the intergranular amorphous region.

IV. DISCUSSION

A. *Yield Stress*

The fall in yield stress with temperature, observed in RHP and Starck $MoSi_2$ (Figure 2), shows that high-temperature deformation in the fine-grained RHP $MoSi_2$ samples responds more to thermal activation. As the temperature is increased, the barrier to dislocation motion due to the Peierls stress decreases in different slip systems because of thermal activation, as a result of which the corresponding CRSS decreases. More dislocation sources are activated at higher temperatures, which may be prevented from operating at lower temperatures due to the higher back stress from dislocations generated. Hence, it is intuitive that the yield stress would decrease. The fine-grained RHP $MoSi_2$ has a higher yield stress compared to Starck $MoSi_2$, when tested at a strain rate of 10^{-3} s^{-1} up to 1200 °C, or at the strain rate of 5×10^{-4} s^{-1} up to 1100 °C. On the other hand, coarse-grained Starck $MoSi_2$, with a SiO_2 content much higher than that of RHP $MoSi_2$, has exhibited higher yield stress at a strain rate of 10^{-3} s^{-1} at 1300 °C and 1350 °C and on testing at the strain rate of 5×10^{-4} s^{-1} at 1200 °C and above. At the strain rate of 10^{-4} s^{-1}, Starck $MoSi_2$ has shown a higher yield stress between 1000 °C and 1350 °C. During deformation at 1200 °C or a lower temperature with the strain rate of 10^{-3} s^{-1}, or at 1100 °C with a strain rate of 5×10^{-4} s^{-1} (that is, with decreasing temperature or at higher temperatures on increasing the strain rate, when diffusion is restricted), the yield strength of RHP $MoSi_2$ is higher as compared to that of Starck $MoSi_2$. The higher strength of RHP $MoSi_2$ is due to the grain boundaries operating as obstacles to dislocation motion and slip transfer between grains, which is the basis of the Hall–Petch relationship. As grain boundaries act as sources of dislocations, a larger grain-boundary area would lead to a higher density of dislocations, which may also result in a higher flow stress. Trends observed in the high-temperature hardness data[6,8] of $MoSi_2$ also follow the Hall–Petch relationship from room temperature to about 1000 °C to 1200 °C. At lower temperatures or higher strain rates, either the thermal energy is too low or time is too short, and not much diffusion is possible in the lattice or at grain boundaries. As a result, diffusion-aided dislocation climb or annihilation is limited. As the temperature is increased or strain rates are reduced, enhanced grain-boundary diffusivity reduces the yield stress in fine-grained $MoSi_2$. Stresses from dislocation pileups are relieved, probably by diffusion-assisted dislocation climb at obstacles,[37] thus reducing the stress required for further dislocation formation and movement. Grain boundaries are sources and sinks of vacancies, which may enhance the rates of dislocation climb. Grain-boundary migration, which operates by climb of grain-boundary dislocations in response to applied stress, is also a possibility. No evidence of grain growth has been observed, however. In the Starck $MoSi_2$, due to its coarse grain size, the area covered by a grain boundary is less, which results in a more gradual decrease of yield stress with increasing temperature or decreasing strain rate.

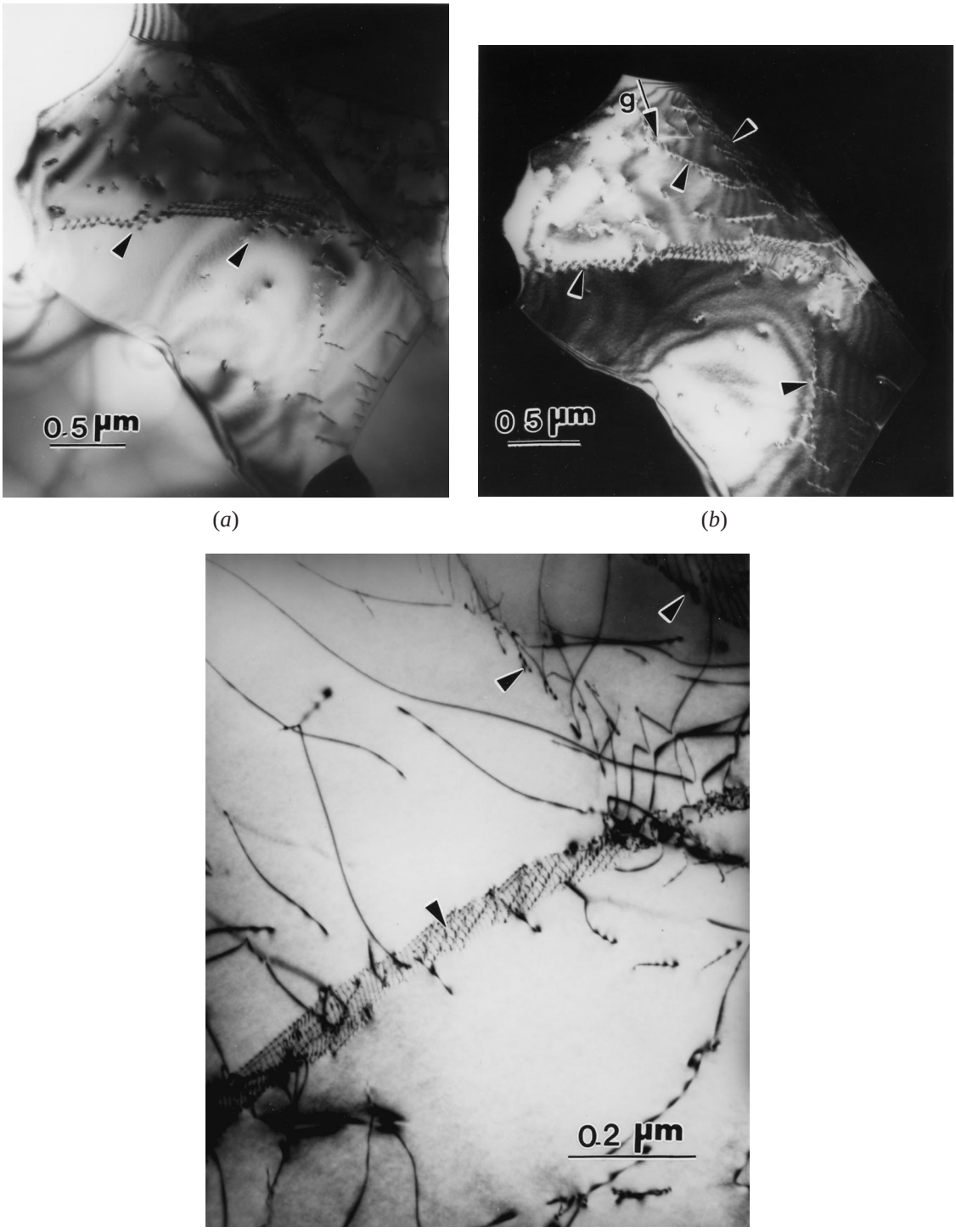

(*a*) (*b*)

(*c*)

Fig. 9—TEM images of low-angle boundaries (arrowed) in RHP $MoSi_2$ deformed at 1200 °C with a strain rate of 10^{-3} s^{-1}: (*a*) bright- and (*b*) dark-field (using the reflection, **g** = [002]) images showing dislocations (arrowed in (a)) emitted or absorbed at low-angle boundaries (arrowed in (b)); and (*c*) bright-field image of lattice dislocations interacting or pinned at with low-angle boundaries (arrowed).

The variation of the natural logarithm of the 0.2 pct yield stress at different temperatures is plotted against the natural logarithm of the corresponding applied strain rates of 10^{-4}, 5×10^{-4}, and 10^{-3} s^{-1} in Figure 13. The strain-rate sensitivities (m, equal to $d \ln \sigma / d \ln \dot{\varepsilon}$) of RHP and Starck $MoSi_2$ at different temperatures in the range of 10^{-3} to 10^{-4} s^{-1}, calculated by estimating the slopes of the plots of the logarithm of the 0.2 pct yield stress with respect to the logarithm of the corresponding applied strain rates (Figure 12), are shown in Table IV. The purpose of choosing the yield point for estimating the strain-rate sensitivity is because the structure characterized by the density of mobile dis-

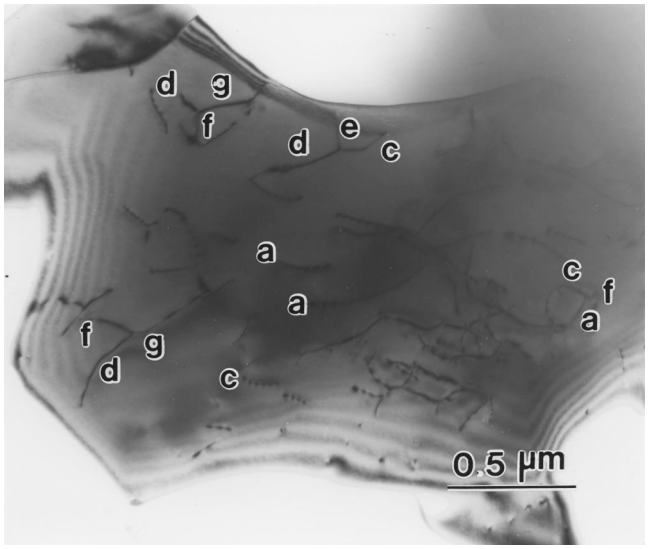

(*a*)

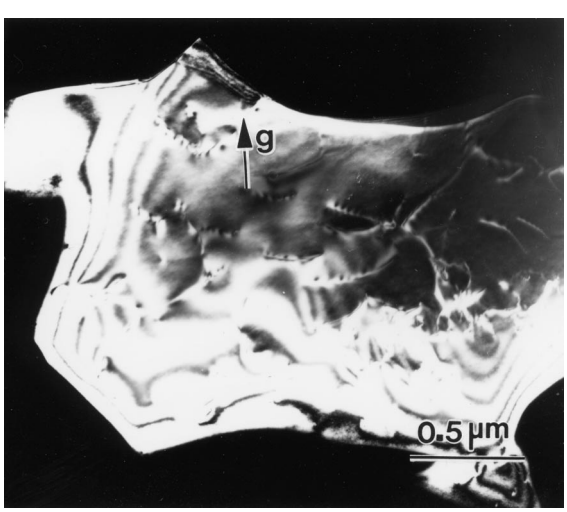

(*b*)

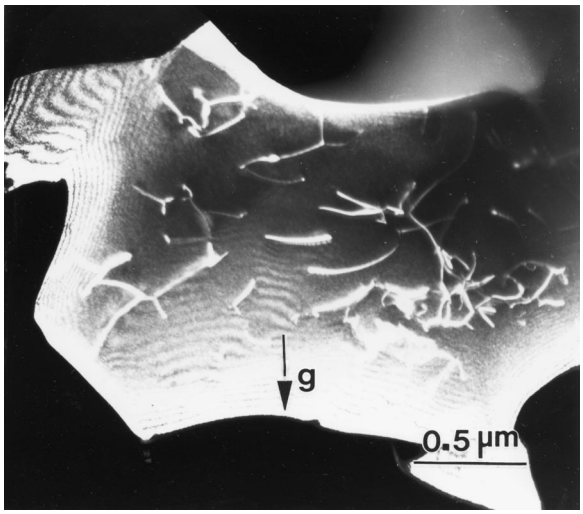

(*c*)

Fig. 10—TEM images of dislocation nodes in RHP $MoSi_2$, tested at 1200 °C with a strain rate of 10^{-3} s^{-1}, recorded under conditions of (*a*) bright field, (*b*) dark field with **g** = [21$\bar{3}$], and (*c*) dark field with **g** = [$\bar{2}$0$\bar{4}$]. The dislocations identified as "a," "c," "d," "e," "f," and "g" are [$\bar{1}$00], [010], ½[$\bar{1}$11], ½[$\bar{1}$11], [$\bar{1}$10], and ½[$\bar{3}$31], respectively.

locations can be assumed to be the same[28] in the samples, even if the temperature or strain-rate-change tests have not been done. Also, the post-yield flow behavior, particularly the plastic strain corresponding to the maximum stress or the onset of softening, has been found to vary sharply with the conditions of testing. At least, the yield point at 0.2 pct plastic strain is distinct in all the flow curves (Figures 3(a) through (c) and 4(a) through (c)). The trend followed by the strain-rate sensitivity shows a sharp increase with increasing temperature in the case of RHP $MoSi_2$ from 0.2 at 1100 °C to 0.63 at 1350 °C, while it does not change much in the case of Starck $MoSi_2$. The higher strain-rate sensitivities of RHP $MoSi_2$ and the significant increase with rise in temperature implies that deformation of fine-grained RHP $MoSi_2$ is strongly affected by thermal activation. A strain-rate sensitivity higher than 0.5, at the grain size of 5.0 μm, is suggestive of superplastic flow characteristics. However, in tension, a fine grain size and strain-rate sensitivity above 0.3 are only necessary, but not sufficient, conditions for superplastic flow. In ceramics, the cohesive strength of grain boundaries is also an important consideration. Even if superplasticity is observed in compression, it is not seen in tension, as the grain boundaries undergo cavitation and fracture at smaller strains. The tendency for grain-boundary cavitation is because of the low fracture energy of grain boundaries. In the present study, RHP $MoSi_2$ deformed to a plastic strain of 34.3 pct (measured from the relation $\varepsilon = \ln (h_0/h_f)$) at 1300 °C with a strain rate of 10^{-3} s^{-1} has not shown any evidence of transgranular or intergranular cracking or cavity formation (Figure 7(a)).

B. *Plastic-Flow Behavior*

1. *Strain hardening or softening*

It is obvious that the strain-hardening behaviors of RHP and Starck $MoSi_2$ depend on temperature and strain rate and

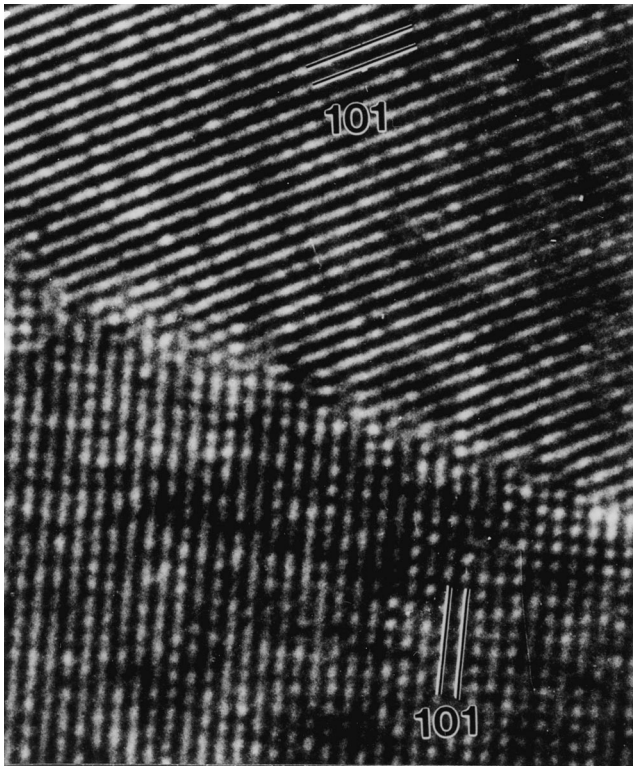

Fig. 11—HRTEM image of a typical grain boundary in RHP $MoSi_2$, which does not show any evidence of amorphous SiO_2 film, after testing at 1200 °C with strain rate of 10^{-3} s^{-1}.

also differ from each other. The strain-hardening characteristics observed in the postyield region of the flow curves of RHP and Starck $MoSi_2$ have been analyzed using the Hollomon equation:[38]

$$\sigma = K\varepsilon^n \qquad [1]$$

and Ludwik equation:[39]

$$\sigma = \sigma_0 + K_1\varepsilon_p^{n_1} \qquad [2]$$

In Eq. [1], σ and ε are the flow stress and strain, respectively, from the true stress–true strain plot; n is the strain-hardening exponent; and K is a constant. In Eq. [2], ε_p is the true plastic strain, σ_0 is the true stress value corresponding to $\varepsilon_p = 0$, K_1 is a constant, and n_1 is the strain-hardening exponent, while σ and ε are the same as in Eq. [1]. Thus, n can be found from the slope of the best-fit line on the plot of log σ *vs* log ε, while n_1 is the slope of the best-fit line drawn on the plots of log $(\sigma - \sigma_0)$ with respect to log ε_p. Equations [1] and [2] suggest that the value of n or n_1 increases with increasing strain hardening and is equal to 0 for an ideally plastic solid. The values of n and n_1 of RHP and Starck $MoSi_2$, calculated from the flow curves, are shown in Tables II and III, respectively. It has been documented[40] that Eq. [2] is more relevant in defining strain-hardening behavior, compared to Eq. [1]. Equation [2] takes into consideration the differences between flow stresses at a certain plastic strain with those at zero plastic strain, and the true plastic strain, by which the strain-hardening effect is magnified. Thus, if n_1 is considered instead of n, the errors introduced due to elastic compliance of the machine are corrected or minimized, because only the plastic, and not the elastic strain is considered. Even if corrections are not made for the elastic compliance of the machine, the comparison of experimental values obtained from the tests on the same machine (such as the INSTRON 8801 or DARTEC machine) with same kind of errors is reasonable and relevant. In addition, the strain-hardening behavior is a characteristic of only the plastically deforming sample. The Al_2O_3 push rod or SiC platens are not expected to undergo any plastic deformation during the tests, which also justifies the use of the stress-strain data to determine the strain-hardening parameters.

In some cases, the plot of log σ – log ε data or those of log $(\sigma - \sigma_0)$ with respect to log ε_0 could not be fitted to a single straight line, but to two different lines, leading to two different values of n and n_1 (Table III). The two different values of n and n_1 are due to sharply different rates of strain hardening at lower and higher plastic strains in Starck $MoSi_2$ at temperatures of 1000 °C and 1100 °C, when the dislocation mobility is low due to high Peierls stress. As the dislocation density is low to begin with, the rate of strain hardening is high. With increasing plastic strain, the dislocation density is increased and, as a result of dislocation rearrangement, the rate of strain hardening falls. The strain-hardening exponent is related to the rate of strain hardening by the relation $d\sigma/d\varepsilon = n(\sigma/\varepsilon)$. The values of n, n_1, and the rate of strain hardening usually decrease with increasing temperature. Figures 5(a) and (b) show that rate of strain hardening of RHP and Starck $MoSi_2$, when tested at the strain rate of 5×10^{-4} s^{-1}, decreases with increasing plastic strain and temperature. There are, however, a few exceptions (data in Tables II and III). (1) In both RHP and Starck $MoSi_2$, the strain-hardening parameters show a significant increase as the test temperature at a strain rate of 10^{-4} s^{-1} is increased from 1000 °C to 1100 °C. (2) At the strain rate of 10^{-3} s^{-1}, the strain hardening rate as well as n are higher when RHP $MoSi_2$ is tested at 1350 °C, compared to that at 1300 °C. (3) Again, in Starck $MoSi_2$ deformed at 10^{-4} s^{-1}, there is a jump in the strain-hardening rate between 1300 °C and 1350 °C. All of these findings could be possible if there is an increase in the dislocation density and a reduction in the mean free path for mobile dislocations, which is the cause of an increase in the SHR. The other possibility is increased dynamic strain aging, discussed in more detail in Section IV–B–3.

The SHR usually falls with decreasing strain rate (Tables II and III), which is explained using the Orowan equation relating dislocation velocity (v) with strain rate ($\dot{\varepsilon}$):

$$\dot{\varepsilon} = \alpha\rho_m \mathbf{b} v \qquad [3]$$

where α is a geometric constant dependent on the orientation of slip systems, ρ_m is the mobile dislocation density, and **b** is the Burgers vector. A higher strain rate may lead to a higher ρ_m value (Eq. [3]) and a smaller mean free path, causing higher stress for dislocation motion and strain hardening. In other words, dislocations are forced to move in a more confined space, which increases the difficulty to bypass obstacles and may reduce dislocation velocity. According to Eq. [3], during tests at a constant strain rate (as in the present experiments), an increase in ρ_m would mean a decrease in v, but conducting the test at a higher strain rate will increase either one or both of them, until a dynamic

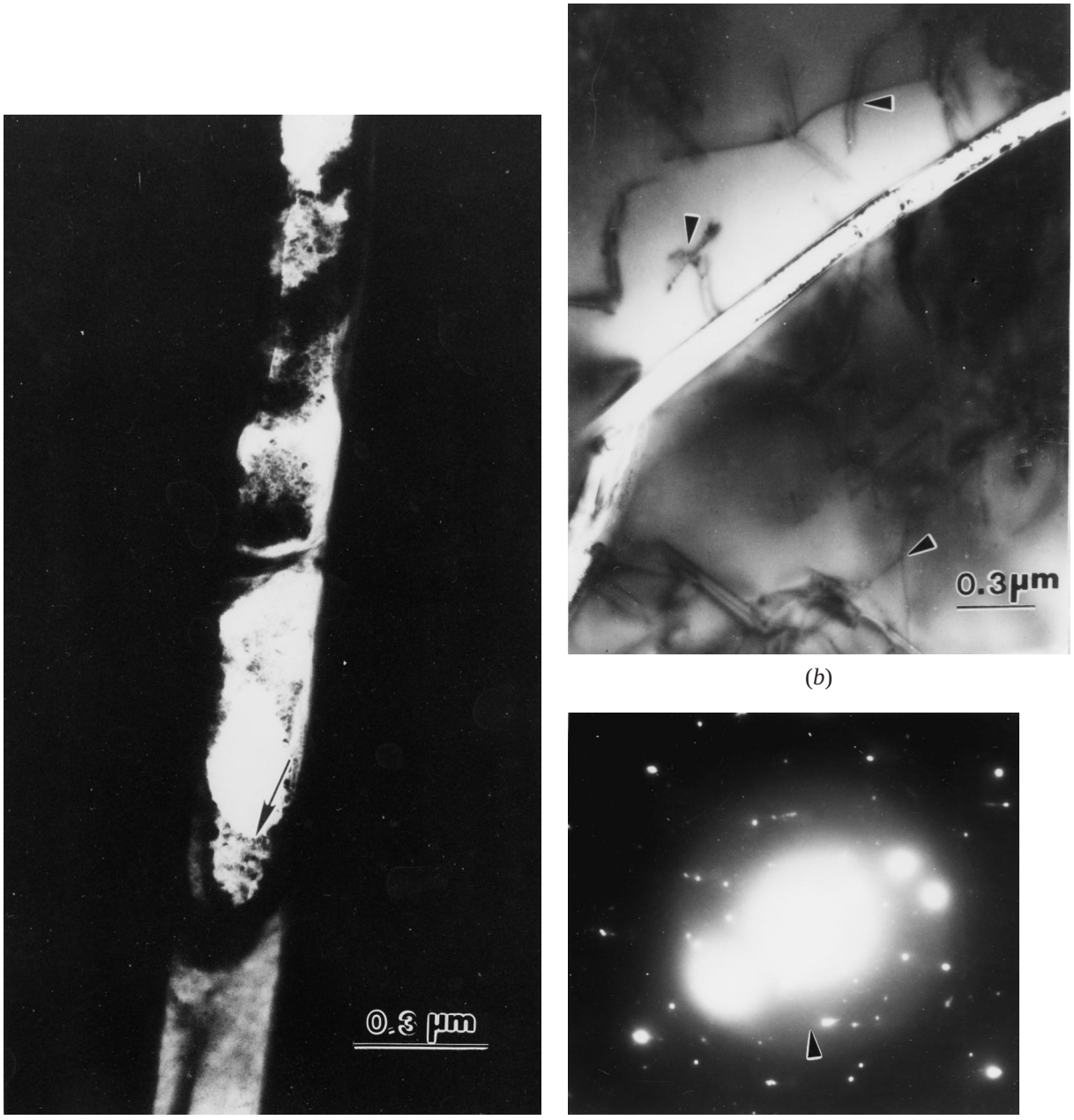

(*a*) (*b*) (*c*)

Fig. 12—Bright-field TEM images of Starck $MoSi_2$ after deformation at 1300 °C with a strain rate of 10^{-3} s^{-1}, showing (*a*) intergranular amorphous SiO_2 film and cracking; (*b*) dislocation nodes near an intergranular crack; and (*c*) electron diffraction pattern with diffuse halo (arrowed), which is characteristic of amorphous SiO_2.

equilibrium is reached. Deformation at a smaller strain rate would allow time for diffusion-assisted dynamic recovery by climb and annihilation of pairs of coplanar dislocations made redundant by the same Burgers vector but having opposite signs and by rearrangement of geometrically necessary dislocations in low-angle boundaries (Figures 9(a) through (c)). As the dislocation density is low inside the subgrains, a larger mean free path is available for mobile dislocations, reducing the degree of strain hardening. The SHRs with plastic strain of RHP and Starck $MoSi_2$, corresponding to 1200 °C and 1300 °C, have been compared in Figures 14(a) and (b), respectively. It is obvious that the strain-hardening rate of fine-grained RHP $MoSi_2$ is greater than that of Starck $MoSi_2$, when tested at a strain rate of 5×10^{-4} s^{-1} at 1200 °C and 1300 °C. On the other hand, on testing at 10^{-4} s^{-1}, RHP and Starck $MoSi_2$ show almost similar strain-hardening characteristics at 1200 °C. However, on testing with a strain rate of 10^{-4} s^{-1} at 1300 °C, the SHR of Starck $MoSi_2$ is distinctly greater than that of RHP $MoSi_2$. The higher SHR of RHP $MoSi_2$ on testing at the strain rate of 5×10^{-4} s^{-1} can be explained by the higher density of dislocations and smaller mean free path for dislocation mobility in the former. Again, the grain boundaries act as barriers to dislocation motion and, at the same time, the ledges are known to be the sources of fresh dislocations. The dislocation density near grain boundaries would be

higher than that at the grain interior in both RHP and Starck $MoSi_2$. Due to the fine grain size of RHP $MoSi_2$, the overall dislocation density would be higher in the absence of a sufficient diffusion-assisted recovery process. At a strain rate of $5 \times 10^{-4}\ s^{-1}$, the recovery due to diffusion at grain boundaries is less dominant as compared to the role of dislocation sources and barriers to dislocation motion. But, at the strain rate of $10^{-4}\ s^{-1}$, the role of grain-boundary diffusion becomes significant, which explains almost similar SHR at 1200 °C and the lower SHR in fine-grained RHP $MoSi_2$ at 1300 °C. It is also intuitive that the vacancy concentration would be higher in the fine-grained RHP $MoSi_2$, because of the higher grain-boundary area and dislocation density, which would also imply a higher rate of recovery compared to Starck $MoSi_2$. It is known that grain boundaries are sources and sinks of vacancies at high temperature.

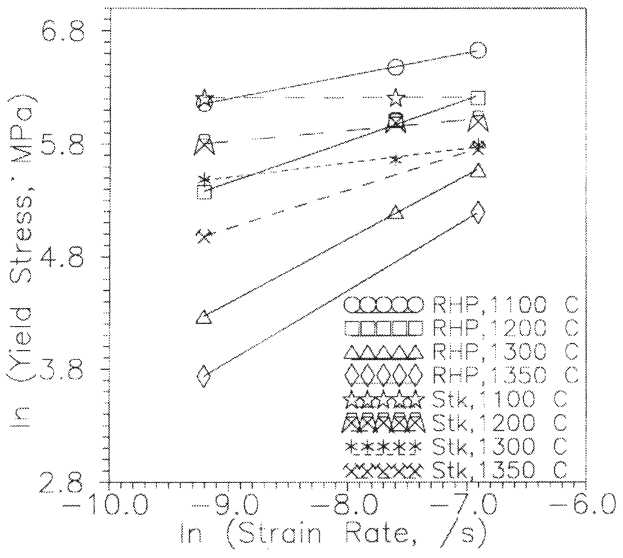

Fig. 13—Plots showing the variation of natural logarithms of yield stress with those of strain rates. Solid lines represent RHP $MoSi_2$, while dashed lines are for Starck $MoSi_2$.

The rate of strain hardening or softening is also expressed in terms of a dimensionless strain-hardening coefficient:[41,42] $\gamma = (1/\sigma)(d\sigma/d\varepsilon)$ or $= d(\ln \sigma)/d\varepsilon$. The values of γ are sensitive to the changes in the rate of strain hardening or softening. According to the condition proposed by Hart,[41] strain hardening or stable flow, in which the increase in cross-sectional area of the sample under compression is commensurate with the change (normally increase) in the flow stress, will be characterized by $\gamma + m \leq 1$, where m is the strain-rate sensitivity and has been explained in Section IV–A. On the other hand, the instability in compression observed during flow softening, which is due to a higher rate of decrease in the flow stress as compared to the increase in cross-sectional area, is characterized by the condition of $\gamma + m \geq 1$. Unstable flow in compression is due to flow localization. The values of γ corresponding to the part of the flow curve at strains corresponding to hardening (γ_H) before reaching maximum stress are negative, while those in the flow curve corresponding to softening (γ_s) are positive. The higher the value of positive γ, the stronger the rate of softening. Thus, the values of γ_s may be used to compare the degrees of softening between samples. Here, γ_s has been computed

Table IV. Table Showing Grain Sizes, Oxygen Content, and Strain Rate Sensitivity, *m*

Materials	Mean Grain Size	Oxygen Content	*m* at 1100 °C (0.60 T_m)	*m* at 1200 °C (0.64 T_m)	*m* at 1300 °C (0.68 T_m)	*m* at 1350 °C (0.71 T_m)
RHP $MoSi_2$	5.0 μm	0.06 wt pct	0.20	0.37	0.57	0.63
Starck $MoSi_2$	27.0 μm	0.89 wt pct	0.03	0.09	0.13	0.34

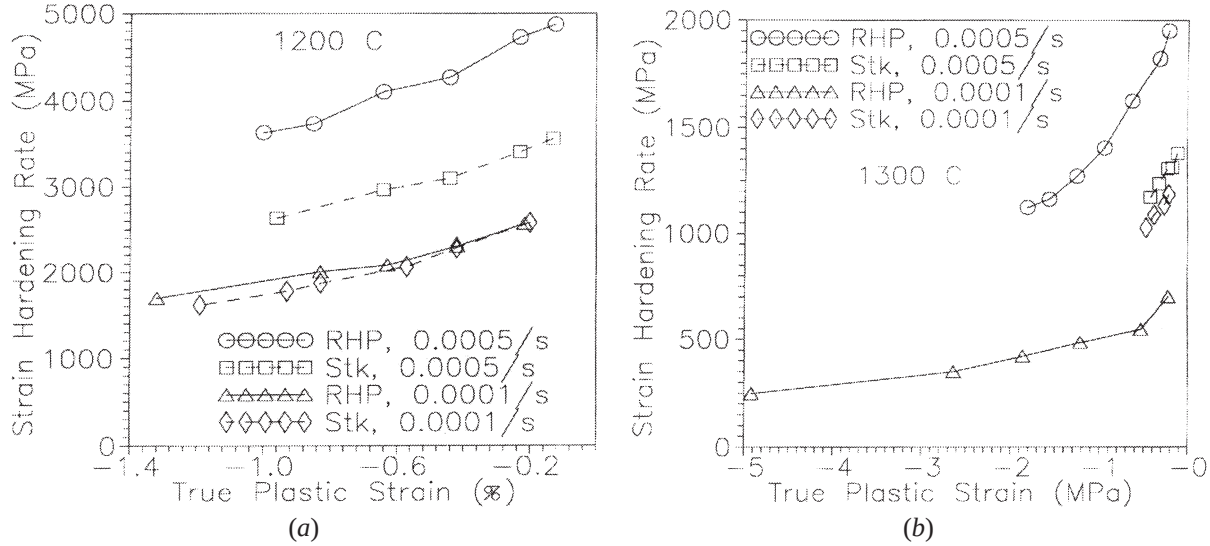

(*a*) (*b*)

Fig. 14—Plots comparing the nature of variation of SHRs, $d\sigma/d\varepsilon$, with true plastic strain, ε_p, of RHP $MoSi_2$ and Starck $MoSi_2$ at (*a*) 1200 °C and (*b*) 1300 °C and strain rates of $10^{-4}\ s^{-1}$ and $5 \times 10^{-4}\ s^{-1}$.

for flow curves obtained from testing using the INSTRON 8801 with $\varepsilon_{p,m} \leq 0.005$ and are presented in Tables II and III. In the RHP $MoSi_2$, the tendency to soften is higher at lower temperatures or higher strain rates. In Starck $MoSi_2$, the softening is more predominant at higher temperatures. Unlike the rates of strain hardening, the rate of softening has been more or less constant with strain, which, of course, is inhomogeneous in the samples (Figures 8 and 12(a) and (b)). The term γ_H could have been used to quantify strain hardening too, but would not be a constant, as the SHR changes with plastic strain (Figures 5(a) and (b) and 14(a) and (b)). In this study, the more widely used parameters (n, n_1, and the average value of the rate of strain hardening ($d\sigma/d\varepsilon$ normalized by G, corrected for temperature)) have been calculated and are shown in Tables II and III.

2. *Plastic strain at maximum stress*

The true plastic strain corresponding to the maximum stress in the flow curve also varies in RHP and Starck $MoSi_2$ with the temperature and strain rate of compression tests. Compression tests do not show necking as in the tension test, but show softening due to dynamic recrystallization, flow localization, or cracking (Figure 8). Tables II and III also show the values of $\varepsilon_{p,m}$ of RHP and Starck $MoSi_2$, respectively.

In the flow curves of RHP $MoSi_2$ corresponding to 1000 °C to 1100 °C and strain rates of 5×10^{-4} and 10^{-4} s^{-1} (Figures 4(b) and (c)) or to 1200 °C and strain rates of 5×10^{-4} s^{-1} (Figure 4(b)) and 10^{-3} s^{-1} (Figure 4(a)) or to 1300 °C and a strain rate of 10^{-3} s^{-1}, the value of $\varepsilon_{p,m}$ is small, and softening is noticed. Dynamic recrystallization is ruled out, as no evidence has been observed in TEM or optical microscopy studies. The part of the flow curve corresponding to initiation of softening is a characteristic of strain or flow localization in some parts of the sample, where the rate of decrease in the flow stress exceeds the rate of increase in the cross-sectional area of the sample. At temperatures as low as 1000 °C or 1100 °C, only four independent slip systems are activated, which is not sufficient for near-homogeneous plastic deformation of any polycrystalline sample. Hence, only those grains which have slip systems with a low CRSS oriented favorably with respect to the stress axis deform more than those, whose slip systems are not oriented favorably. In $MoSi_2$, the magnitude of the Peierls stress for operation of the $\{013\}\langle 331\rangle$ slip system is orientation dependent, particularly if the normal to the slip plane is close to the [001] direction. As dislocation pileups form at grain boundaries, the stress concentration needs to induce formation of geometrically necessary dislocations in the neighboring grains in order to maintain continuity.[43,44] Otherwise, stresses need to be relieved by microcrack formation or dynamic recovery. Dynamic recovery may not be the dominant process in the absence of slower kinetics of diffusion at lower temperatures or with less time allowed at higher strain rates. The previous mechanism explains why softening takes place up to 1100 °C at the strain rates of 10^{-4}, 5×10^{-4}, and 10^{-3} s^{-1} and at 1200 °C, when strain rates are 5×10^{-4} and 10^{-3} s^{-1}.

However, softening is hardly observed when the RHP $MoSi_2$ samples are deformed at 1200 °C or above at the strain rate of 10^{-4} s^{-1} (Figure 3(c)). As the temperature is increased or the strain rate is reduced, a typical post-yield flow curve is characterized by plastic strain increasing uniformly through the specimen without much alteration in the flow stress, which is responsible for lower SHRs due to dynamic recovery. The mechanism of dynamic recovery has been explained, while discussing strain hardening. An equilibrium is reached between dislocation formation or multiplication and their annihilation or absorption at grain boundaries, leading to a stable substructure with almost constant subgrain size. As a result of a stable substructure, the flow is stabilized and the trend to soften is reduced. The fact that $\varepsilon_{p,m}$ increases with increasing temperature or slower strain rate is consistent with the fact that the subgrain size increases and, so, the mean free path for dislocation movement increases too. The subgrain boundaries interact with or pin lattice dislocations, acting as obstacles to dislocation movement (Figure 9(b)). A stable substructure is not developed in all the grains when there is not enough diffusion, such as the situation of a high strain rate or low temperature, which may also be the reason for flow localization.

In Starck $MoSi_2$, the flow curve corresponding to the deformation using a strain rate of 10^{-4} s^{-1} at 1000 °C (Figure 4(c)) shows a relatively large $\varepsilon_{p,m}$ value, which is in contrast to the flow behavior of RHP $MoSi_2$ under similar conditions (Figure 3(c)). At a given strain rate, $\varepsilon_{p,m}$ decreases with increasing temperature, followed by a tendency toward strain softening. The variation of $\varepsilon_{p,m}$ with strain rate does not appear to follow a definite trend. The difference between σ_y and σ_{max} in the flow curve is at its maximum at 1000 °C and 1100 °C and decreases sharply with increasing temperature.

In Starck $MoSi_2$, the grain size is significantly coarse and the grain boundaries play a smaller role, except when the temperature is increased and the strain rate is small, with the temperature playing a more important role. It takes a higher plastic strain for the dislocation density to increase to a level (when the recovery process is initiated) which increases $\varepsilon_{p,m}$. However, as the temperature is increased, the diffusivity is higher, and dynamic recovery and an increase in $\varepsilon_{p,m}$ are expected. The decrease in $\varepsilon_{p,m}$ with increasing temperature is in contrast to that expected and observed in the RHP $MoSi_2$. The increasing γ_s or rate of softening at strains greater than $\varepsilon_{p,m}$, on testing at 1300 °C with a strain rate of 5×10^{-4} s^{-1}, is strong evidence of the tendency of flow localization. The SiO_2 particles inside the grains and at the grain boundaries soften and flow (Figure 12(a)), as a result of which deformation is localized. The higher the temperature, the stronger is the possibility that SiO_2 would soften at a smaller bulk sample strain and, as a result, the greater the probability of flow localization. However, the yield point is not adversely affected at the 1200 °C to 1350 °C range of temperatures, as plastic deformation by dislocations inside the $MoSi_2$ grains is responsible for yielding in Starck $MoSi_2$. The intergranular SiO_2 begins to soften as the stress concentration is allowed to build up at the grain boundaries.

The fact that σ_{max}/σ_y follows the same trend as $\varepsilon_{p,m}$ for both RHP $MoSi_2$ (Table II) and Starck $MoSi_2$ (Table III) is mainly, because a larger fraction of the flow curve represents strain hardening when $\varepsilon_{p,m}$ is large, and *vice versa*. Even if the SHR decreases with increasing temperature in RHP $MoSi_2$ due to dynamic recovery, σ_{max}/σ_y increases, showing its dependence on the rate of strain hardening as well as on $\varepsilon_{p,m}$.

3. *Serrated plastic flow*

Serrations can be observed in the flow curves of both RHP and Starck $MoSi_2$. The flow curves corresponding to deformation of RHP $MoSi_2$ at a strain rate of 10^{-3} s^{-1} and temperatures of 1200 °C and 1300 °C (Figure 3(c)) and to that of Starck $MoSi_2$ at 1300 °C and the strain rates of 10^{-3} s^{-1} (Figure 4(c)) and 5×10^{-4} s^{-1} (Figure 6) recorded during tests on the DARTEC machine have shown systematic serrations occurring quasi-periodically. The periodically appearing major load drops (shown with arrows) along the flow curve have been considered, in this study, to be serrations forming due to dislocation dynamics during deformation. The finer details of serrated plastic flow could not be distinguished from the continuous oscillations due to the higher levels of electronic noise of the DARTEC test system. The electronic noise in machines like DARTEC may also form a band in the flow curves. So, experiments need to be repeated on a screw-driven rigid machine. But, the major load fluctuations (arrows in Figures 3(c), 4(c), and 6)) are more likely serrations originating from the behavior of the deforming specimen, than anything else.

The cause of serrations in the flow curve has been reported to be due to the sudden changes in the velocity or density of mobile dislocations with the application of stress. In polycrystalline $MoSi_2$, the dislocation density in many grains can be assumed to be low to begin with, in agreement with some of the past studies. With the onset of yielding and increasing stress, the velocity and density of mobile dislocations increase abruptly to match the strain rate. This can explain the yield-point phenomenon, but does not address the issue of jerky or serrated flow behavior. One of the causes could be the pinning of dislocations by an environment of solute atoms around the dislocation core, which is termed dynamic strain aging, or the Portevin–Le Chatlier effect. The viscous drag on mobile dislocations is maximized at a certain combination of strain rate and temperature, when the dislocation velocity is matched by the diffusivity of solute atoms. *In-situ* dynamic TEM straining experiments[23] on single crystals of $MoSi_2$, NiAl, and TiAl have shown that dislocations move in a viscous manner. It has been reported[24] and follows, from estimations using a relationship derived by Hirth and Lothe,[45] that an interstitial impurity concentration in excess of 1000 wppm (0.1 wt pct) is necessary to yield an appreciable drag of solute atmospheres to dislocation mobility and flow stress. Experiments[15] have demonstrated that serrated flow occurs in samples with as small as a 300 wppm impurity concentration. A model[46] originally based on calculations for NiAl and proposed by Messerschmidt *et al.*[23] for intermetallics in general, implies that irrespective of impurity concentration, the energy of the dislocation core in the intermetallics is reduced by an atmosphere of intrinsic point defects, such as vacancies or anti-site defects in one or both of the sublattices. Positron annihilation studies by Ito *et al.*[25] have shown that the concentration of thermally induced Si vacancies increases sharply on heating to and above 800 °C. As a result, the intrinsic point-defect atmosphere at the dislocation core, when the dislocation moves, is compelled to drag the defect atmosphere. The drag on the dislocation movement, which probably maximizes at or is high at some strain rates and temperatures, is not characterized by a critical strain or a critical vacancy concentration. In the present situation, the interstitial impurity atoms in RHP and Starck $MoSi_2$ are C, N, and O (O not present as SiO_2) (Table I). The total concentration of interstitial impurities is close to or slightly less than 1000 wppm. It is likely that both pinning due to impurities as well as a high concentration of intrinsic point defects may be contributing to the occurrence of serrated plastic deformation. Lothe[47] has shown that an interstitial impurity atmosphere creates a Peierls-type barrier for dislocation glide, which is also expected for a concentration of point defects around the dislocation core. Activation volumes calculated from the results of constant-load compression creep tests[48] at 1200 °C, performed by incrementing loads, have been found to be $2\mathbf{b}^3$ and $27\mathbf{b}^3$, which further suggests that dislocations in both RHP and Starck $MoSi_2$ encounter a Peierls-type barrier. On the basis of dynamic *in-situ* TEM studies on deformation of ⟨201⟩-oriented single-crystal $MoSi_2$ samples at 990 °C, Messerschmidt *et al.*[23] have reported that dislocations with $\mathbf{b} = \frac{1}{2}\langle 111 \rangle$ move either by shifting superkinks or by taking curved shapes. Both kinks and gentle curvatures in dislocations, which are mostly straight (crystallographic directions have not been determined), can be observed in Figure 9(c). Mostly straight dislocations suggest that those are restricted to Peierls valleys. The dislocations could be divided into segments, each of which is lying between a couple of pinning points. The curvatures in the dislocations suggest that under stress, dislocations tend to bow out between pinning points such as solute atoms, dislocation nodes, as well as low-angle boundaries.

Serrated plastic flow in $MoSi_2$ single crystals[13,15,24] has been found to be also associated with a negative strain-rate sensitivity, high rate of strain hardening, and anomalous increase in the flow stress. In all the cases, the conditions for an anomalous increase in the CRSS and serrated flow behavior have shown variations with the types of slip systems activated, strain rates, and temperatures. The temperature range of anomalous increases in flow stress has been found to increase to a higher slot upon an increase in the strain rate. A similar behavior is expected to accompany the plastic flow of polycrystalline $MoSi_2$ as well. In polycrystalline $MoSi_2$, serrated plastic flow has not been reported, either because the temperature range for serrated plastic flow is lower than the BDTT, or the defect or solute drag on dislocations is small. At high temperatures and low strain rates, the lattice diffusivities of solute atoms and point defects are high, lowering the drag on mobile dislocations. So, serrations do not appear in the flow curves. In this investigation, serrations are more obvious in the 10^{-3} s^{-1} tests in the 1200 °C to 1300 °C range in the fine-grained RHP $MoSi_2$ and at 1300 °C in Starck $MoSi_2$ than at lower strain rates.

Strain-rate or temperature-change tests at a particular strain and dislocation substructure are required to investigate the negative strain-rate sensitivity. Strain-rate-jump tests could not be performed on the INSTRON 8801 or DARTEC machines used in this study, due to unavoidable limitations in the machine software, and need to be carried out on a different type of testing system. Again, in this study, serrations are not necessarily in the flow curves with high rates of strain hardening. In addition to being present in the flow curves showing little or no softening (Figure 3(a): RHP $MoSi_2$, 1300 °C, 10^{-4} s^{-1}), serrations are also found in the parts of

flow curves corresponding to softening, which implies that regions of samples experiencing localized deformation also show serrated flow.

The drops in stress at intervals of plastic strain in the serrated flow curves of RHP $MoSi_2$ (Figure 3(c)) and Starck $MoSi_2$ (Figures 4(c) and 6) have been further analyzed. Serration heights corresponding to a certain plastic strain can be quantified in terms of the ratio of the stress at the bottom or lowermost point of the serration (σ_L) to that at the top or uppermost point (σ_U) at a particular plastic strain. The smaller the serration-stress ratio (σ_L/σ_U), the larger the height of the serration. The ratio σ_L/σ_U is related to the ratio of the corresponding mobile dislocation densities as[49]

$$\sigma_L/\sigma_U = \tau_L/\tau_U = (\rho_U/\rho_L)^{1/m'} \quad [4]$$

where ρ_U and ρ_L are the densities of mobile dislocations at the uppermost and lowermost point of serrations, respectively, and m' is the dislocation-velocity stress exponent. Equation [4] is derived from combining Eq. [3] and the relation proposed by Gilman and Johnston[50,51] for dislocation velocity as a function of the applied shear stress:

$$v = (\tau/\tau_0)^{m'} \quad [5]$$

where τ_0 is the resolved shear stress corresponding to unit velocity. Figure 15(a) shows the variation of serration-stress ratios with compressive plastic strain in the flow curves of RHP $MoSi_2$ corresponding to the tests conducted at 1200 °C and 1300 °C and a strain rate of 10^{-3} s^{-1}. Figure 15(b) shows the variation of serration-stress ratios with compressive plastic strain in the flow curves of Starck $MoSi_2$ corresponding to the tests conducted at 1300 °C, with strain rates of 10^{-3} and 5×10^{-4} s^{-1}. In Figure 6, which shows the load-displacement curve of Starck $MoSi_2$, corresponding to deformation at 1300 °C with a strain rate of 5×10^{-4} s^{-1}, there is a likelihood of confusion regarding which stress drops to choose. The serrations with σ_L/σ_U closer to the average value have been chosen, and those differing by more than 30 pct with either of the neighboring serrations have not been considered. In both RHP and Starck $MoSi_2$, the serration-stress ratio is found to decrease with an increase in plastic strain. In other words, the magnitude of the stress drops increases with increasing plastic strain. The serration-stress ratios of RHP $MoSi_2$ corresponding to the 1200 °C test are more than those corresponding to the 1300 °C test (Figure 15(a)), which also implies that the stress drops are more at 1300 °C. The lower serration-stress ratios or higher stress drops observed at 1300 °C compared to those at 1200 °C is probably, because of the higher equilibrium vacancy concentration as well as higher diffusivity of point defects or interstitial impurities at higher temperatures, which increases the drag on gliding dislocations. In case of tests conducted at 1300 °C on Starck $MoSi_2$, the serration-stress ratios are higher or the stress drops are smaller for a strain rate of 10^{-3} s^{-1} as compared to those at 5×10^{-4} s^{-1} (Figure 15(b)), implying that there is also a strain-rate effect on the solute or point-defect drag on gliding dislocations. The drag on gliding dislocations is more intense at the slower strain rate of 5×10^{-4} s^{-1}, because of the increased time allowed for diffusion.

The intervals between consecutive serrations in the flow curves of RHP and Starck $MoSi_2$ corresponding to the tests using the DARTEC machine have also been measured and plotted against true compressive plastic strain, as shown in Figures 16(a) and (b), respectively. In RHP $MoSi_2$, tested at 1300 °C and a strain rate of 10^{-3} s^{-1} (Figure 3(c)), serrations of the type considered here can be distinguished after some degree of plastic straining ($\varepsilon_\rho = 0.16$), which explains the shift in the plot (Figure 16(a)) of the interval between serrations against plastic strain at 1300 °C with respect to that at 1200 °C. It is interesting to note that the magnitude of plastic-strain intervals between consecutive stress drops or serrations decreases continuously with increase in the true plastic strain, which can be explained from the increase in the concentration of vacancies with increase in plastic strain and with increasing mobile dislocation density. Although there is only a small overlap of data for a given plastic strain, the plastic-strain intervals for the occurrence of stress drops during the test on RHP $MoSi_2$ at 1300 °C is larger than those corresponding to the test at 1200 °C (Figure 16(a)). Again, the plastic-strain interval for the occurrence of serrations during tests on Starck $MoSi_2$ at 1300 °C is larger for the strain rate of 5×10^{-4} s^{-1}, when compared to that recorded at the strain rate of 10^{-3} s^{-1} (Figure 16(b)). In other words, the plastic-strain intervals between two consecutive serrations are dependent on the rate of strain hardening and extent of diffusion allowed in the $MoSi_2$ lattice. Probably, at the higher temperature of 1300 °C, compared to 1200 °C (in the case of RHP $MoSi_2$, as in Figure 16(a)) or at the slower strain rate of 10^{-4} s^{-1} compared to 5×10^{-4} s^{-1} (in the case of Starck $MoSi_2$, as shown in Figure 16(b)), strain hardening is less (Figures 14(a) and (b)), because the dislocation density is reduced by annihilation and low-angle boundary formation. As a result, a higher plastic-strain interval is necessary between consecutive stress drops or a sudden increase in the mobile dislocation density. If the strain hardening is more, the dislocation density is higher and the effect of drag on dislocations by solutes or point defects on flow stress is more visible and is expected to occur at smaller plastic-strain intervals.

On examination of the trends followed in the mechanical behavior or TEM deformation substructures in $MoSi_2$, it is intuitive to suggest four other alternative mechanisms which could be contributing in different magnitudes to the occurrence of serrated plastic flow, other than solute or point-defect dislocation interaction. The following mechanisms also justify the observation of the decrease of the serration-strain interval with increasing plastic strain or rate of strain hardening. The first of these is the interaction of lattice dislocations with low-angle boundaries (Figures 9(a) through (c)). A higher rate of strain hardening at a lower temperature or higher strain rate would correspond to a smaller subgrain size. If serrations are due to pinning and the subsequent release of lattice dislocations by the subgrain boundaries, it is expected that the strain intervals of serrations would depend on the subgrain size. As the subgrain size is reduced, the frequency of serrations would increase. The second possible mechanism involves pinning and unpinning of dislocations at dislocation nodes (Figures 10(a) through (c)), which might have also contributed to serrated flow. The probability of the formation of dislocation nodes increases with increasing plastic strain or increased rate of strain hardening, as the mean free path for mobile dislocations decreases and the application of stress

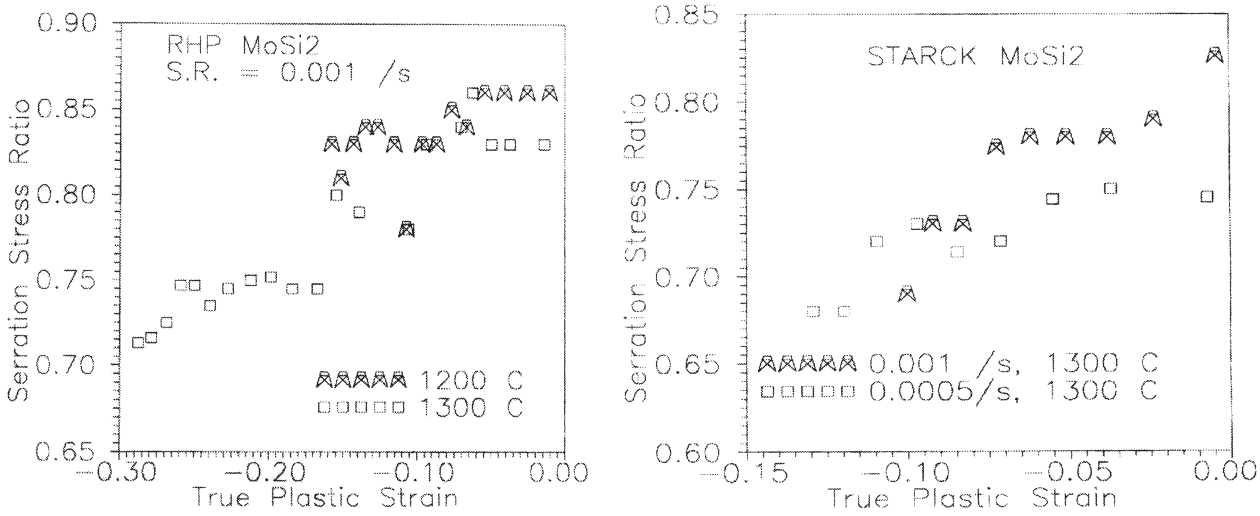

Fig. 15—Plots showing variation and comparison of serration stress ratios with true plastic strain in (*a*) RHP $MoSi_2$ at 1200 °C and 1300 °C on testing at the strain rate of 10^{-3} s^{-1} and (*b*) Starck $MoSi_2$ at 1300 °C on testing at strain rates of 10^{-3} s^{-1} and 5×10^{-4} s^{-1}.

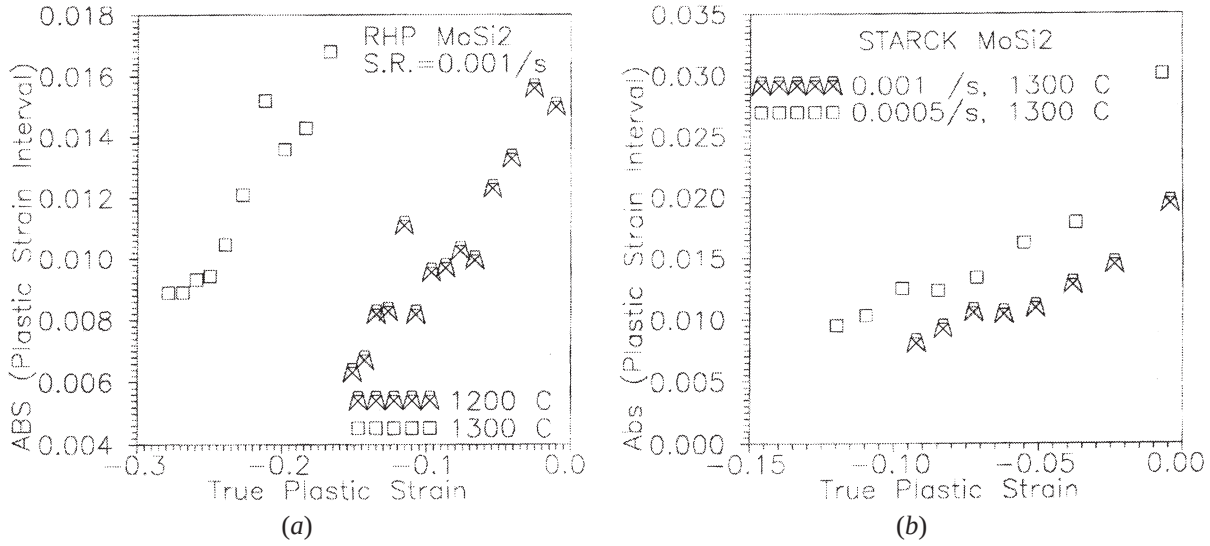

Fig. 16—Plots showing the variation of plastic strain intervals between consecutive stress drops with increment in the true plastic strain in (*a*) RHP $MoSi_2$ and (*b*) Starck $MoSi_2$.

leads to unpinning of dislocations at nodes. The third possible mechanism is the interaction of Si vacancies and solute atoms with jogs on screw dislocations,[49] which pin the dislocations and move in a nonconservative manner by thermal activation with rising test temperatures. The presence of vacancies aids in the motion of jogs and a reduction in the required shear stress. Again, excess vacancies or interstitials are created by the nonconservative movement of jogs upon application of a sufficiently high shear stress, which will lead to a drop in flow stress subsequently. With increasing plastic strain, the vacancy concentration is likely to increase, causing serrations more frequently. The fourth alternative mechanism, more likely to operate in RHP $MoSi_2$ at high temperatures, is due to the increased ability of stress reduction at the junction of high-angle grain boundaries and dislocation pileups by climb of the lead dislocation along grain boundaries. Observations on grain-boundary shear stimulated by intragranular slip, interaction between lattice and grain-boundary dislocations, and motion of grain boundary dislocations by glide and climb has been reported in the literature[44,52] and modeled.[53] If the applied stress is increased, the number of dislocations in the pileup increases, triggering further dislocation climb and movement of grain boundaries, followed by a fall in stress. With increasing plastic strain and vacancy concentrations, recovery by climb at grain boundaries would occur more frequently. The magnitude of the stress drops is also likely to increase with increasing plastic strain in this mechanism, as grain-boundary mobility by dislocation climb is supposed to rise with increasing vacancy concentration. Further work is necessary to analyze the effect of all the afore-mentioned mechanisms.

C. *Studies of Deformed Samples*

As there are a great deal of literature data on the dislocation structures of $MoSi_2$ deformed at 1200 °C and above with strain rates of 10^{-4} s^{-1} or smaller, samples deformed at a strain rate of 10^{-3} s^{-1} have been chosen for microstructural studies in this work to extend the understanding of deformation behavior to the higher strain rates used in this study. It is important to note that the grain size and orientation of individual grains with respect to the stress axis plays an important role during deformation of $MoSi_2$ at temperatures of 1200 °C or lower and at the high strain rate of 10^{-3} s^{-1} in the evolution of dislocation substructure.

The microstructures of deformed samples of RHP $MoSi_2$ with a 5 μm grain size, in agreement with trend followed by corresponding flow curves, has not shown evidence of cracking-induced softening at 1200 °C, when tested with a strain rate of 10^{-4} s^{-1}, or at higher temperatures with strain rates of 10^{-3} s^{-1}, as well. Transgranular cracking is more prevalent at lower temperatures, because of the fact that in certain grains, only a restricted number of slip systems are activated, while in some neighboring grains, a larger number of slip systems are activated. In order to maintain continuity across the grain boundary, geometrically necessary dislocations are required to be generated.[43] If the individual grain orientation is "hard," that is, the CRSS of the slip system is higher than the fracture stress, cracking may take place along cleavage planes. Chang *et al.*[7] have reported extensive cracking in samples tested at and below 1000 °C, but not in those tested at 1100 °C or above.

The flow curves show dynamic recovery to be the dominant mechanism at 1300 °C and also at 1200 °C, as the strain rate is reduced to 10^{-4} s^{-1}. At a higher strain rate (such as 10^{-3} s^{-1}) of testing at 1200 °C, low-angle boundaries formed by dislocation climb have been observed in the microstructure (Figures 9(a) through (c)), but the corresponding flow curves (Figures 3(b) and (c)) have not shown dynamic recovery as the predominant mechanism. Figures 9(a) through (c) show that low-angle boundaries act as sources or sinks of lattice dislocations as well as interact with lattice dislocations, the mechanisms of which have been discussed by Hirth.[44] When a lattice dislocation interacts with a low-angle grain boundary, steps and dislocation nodes may form at a grain boundary, followed by a relaxation of long-range stresses through redistribution by climb at high temperatures.

Both low-angle boundaries and dislocation nodes are observed inside the same grain in Figure 9(c). It has been observed during a detailed study of the specimen that some grains are more likely to show formation of low-angle boundaries, while some others have a different dislocation substructure consisting of dislocation nodes (Figures 10(a) through (c)), which implies that the deformation mechanisms vary with grain size and orientation of the individual grains with respect to the stress axis. The dislocation reactions D1 ($[\bar{1}00] + [010] \rightarrow [\bar{1}10]$), D2 ($\frac{1}{2}[111] + [\bar{1}00] \rightarrow \frac{1}{2}[\bar{1}11]$), and D3 ($\frac{1}{2}[\bar{3}31] \rightarrow \frac{1}{2}[\bar{1}11] + [\bar{1}10]$), listed also in Section III–B–3, are energetically favorable. Dislocation nodes and similar reactions (as in reactions D1 through D3) have been reported in the past in polycrystalline $MoSi_2$ samples deformed at temperatures in, or lower than, the 1200 °C to 1300 °C range and at strain rates of 10^{-4} s^{-1} in samples with a coarser grain size. The reaction D1 has also been observed in polycrystalline $MoSi_2$ samples tested at a strain rate of 10^{-4} s^{-1} at 1100 °C and 1200 °C, or in samples deformed by indentation between 600 °C and 1000 °C. The dislocation reaction D2 has been reported in polycrystalline $MoSi_2$ samples tested using hardness indentation at 800 °C. The dislocation reaction D3 has been observed by Maloy *et al.*[19] in [001]-oriented single crystals, compression tested at 1000 °C using a strain rate of 10^{-5} s^{-1}. The decomposition of $\langle 331 \rangle$ leads to a 33.3 pct reduction in energy. The afore-mentioned dislocation reactions are characteristic of those formed at low temperatures, and the reaction D3 has been reported to play an important role in the hard [001] orientation.

The interdislocation intersections and node formations (Figure 12(b)) in Starck $MoSi_2$ grains, similar to those observed in RHP $MoSi_2$ (Figures 10(a) through (c)), indicate that the pinning of lattice dislocations by the mechanism of a dislocation-dislocation reaction leads to strain hardening. Unlike those of the RHP $MoSi_2$, the flow curves of Starck $MoSi_2$ (Figures 4(a) through (c)) have not shown clear evidence to suggest dynamic recovery as the predominant mechanism with increasing temperature or decreasing strain rate. Low-angle boundaries have been found in isolated areas, which suggest that some degree of dislocation-climb-controlled recovery takes place. But, the major factor in deformation of Starck $MoSi_2$ is softening of SiO_2 particles and viscous flow in the form of an intergranular film (Figure 12(b)), which cracked by shear as the specimen was continuously strained. Thus, the softening of SiO_2 in Starck $MoSi_2$ is more detrimental during its postyield flow behavior than at yielding.

Transgranular (Figure 7(b)) and intergranular (Figures 12(a) and (b)) cracking take place in the coarse-grained Starck $MoSi_2$ after a 10 pct plastic strain, when deformed at 1300 °C with a strain rate of 10^{-3} s^{-1}, which has been the cause of softening (Figure 4(c)). Transgranular microcracking has been reported[8] in coarse-grained $MoSi_2$ tested at 1400 °C.

It may be argued that some of the dislocation substructure discussed earlier could have existed in an as-hot-pressed sample. It appears unlikely to be true, as TEM studies on an as-hot-pressed RHP $MoSi_2$-20 vol pct SiC composite[6] with a matrix grain size of 18 μm, a Starck $MoSi_2$-20 vol pct composite[53] with a matrix grain size of 5 μm, or a Starck $MoSi_2$-5.5 at pct A1 alloy[54] with a matrix grain size of 25 μm have not shown a dislocation substructure constituting of a frequent occurrence of low-angle boundaries. During the hot-pressing operation, the static uniaxial pressure of 26 MPa is released soon after consolidation at 1500 °C (RHP $MoSi_2$ and composites) or at 1600 °C to 1700 °C (Starck $MoSi_2$ and its alloys or composites) for 1 hour. The applied stress is accommodated by diffusion, mass transfer, and volume shrinkage of closed or open porosities, constituting the process of densification. Deformation by dislocation movement and multiplication inside individual grains can take place only after significant densification and is constrained during uniaxial pressing inside the die. That explains why the dislocation density has been found to be low in the as-hot-pressed samples discussed previously as well as in the literature, particularly in monolithic $MoSi_2$ samples.[7] Dislocation generation is, however, expected at the

$MoSi_2$-SiC interfaces in the composites, because of a mismatch in the coefficient of thermal expansion. Low-angle boundary formation under static recovery conditions[55] needs a sufficiently high density of dislocations for the generation of high interdislocation interaction stresses, which act as a driving force for dislocation rearrangement.

V. CONCLUSIONS

The following conclusions can be drawn from the present study.

1. The yield strength of RHP $MoSi_2$ with an average grain size of 5 μm is higher than that of Starck $MoSi_2$ with a grain size of 27 μm, when tested at a strain rate of $10^{-3}s^{-1}$ up to 1200 °C or at 5×10^{-4} s^{-1} up to 1100 °C, implying that grain boundaries lead to higher yield strength under those conditions. At higher temperatures or smaller strain rates, the fine-grained RHP $MoSi_2$ demonstrates a lower yield strength, showing the effect of increased grain-boundary mobility. In spite of the high silica content, Starck $MoSi_2$ has shown a higher yield strength at 1300 °C as compared to RHP $MoSi_2$ and $MoSi_2$-20 vol pct SiC composites with an average matrix grain size of 5 μm, when tested in the strain-rate regime of 10^{-3} to 10^{-4} s^{-1}. The previous study shows the paramount importance of grain size in defining the high-temperature strength of $MoSi_2$.
2. The strain-rate sensitivity of the fine-grained RHP $MoSi_2$ is not only higher than that of coarse-grained Starck $MoSi_2$, but also increases sharply with an increase in temperature in the strain-rate regime of 10^{-3} to 10^{-4} s^{-1}. The deformation of RHP $MoSi_2$ is subjected to a higher degree of thermal activation, compared to that to Starck $MoSi_2$.
3. The strain-hardening behavior also varies with temperature, strain rate, and grain size. Also, strain hardening can be distributed into two regimes, one showing a higher rate of hardening as compared to the next, which proceeds in parallel with the process of dynamic recovery.
4. The true plastic strain at maximum stress is found to increase in RHP $MoSi_2$ with increasing temperature at each strain rate of testing due to the mechanism of dynamic recovery, which, along with the high strain-rate sensitivity, is evidence of the high compressive ductility of fine-grained RHP $MoSi_2$. In Starck $MoSi_2$, the true plastic strain at maximum stress decreases with increasing temperature, as the flow is localized at the grain-boundary SiO_2 particles, which soften and flow in a viscous manner to form intergranular films.
5. Serrated plastic flow has been observed during deformation with a strain rate of 10^{-3} s^{-1} in the range of 1200 °C to 1300 °C and also at smaller strain rates in both RHP and Starck $MoSi_2$. The serration heights increase with increasing plastic strain. The interval between consecutive serrations also decreases with the increase in plastic strain. The serrations are not characterized by a critical strain for the onset, but surely depend on the strain rate and temperature. The interaction of point defects and solute atmospheres with mobile dislocations possibly leads to serrated plastic-flow behavior. Further research is needed in this area.
6. The TEM microstructures of RHP $MoSi_2$, deformed at 1200 °C to 18.4 pct strain with a strain rate of 10^{-3} s^{-1}, have shown evidence of dynamic recovery by low-angle boundary formation and lattice dislocations being emitted or absorbed at the boundaries. Not all grains show low-angle boundary formation, and dislocation-node formation also takes place. Dislocation reactions observed in the nodes during deformation at a strain rate of 10^{-3} s^{-1} and 1200 °C are consistent with the observations cited in the literature for slower strain rates and temperatures equal to or lower than 1200 °C. Dislocation-network formation could be one of the mechanisms of work hardening.
7. The formation of low-angle boundaries and dislocation nodes has also been observed in Starck $MoSi_2$, when deformed at 1300 °C with a strain rate of 10^{-3} s^{-1}. Starck $MoSi_2$ has shown evidence of SiO_2 film formation at grain boundaries on deformation at 1300 °C with a strain rate of 10^{-3} s^{-1}, which leads to postyield softening, intergranular crack initiation, and fracture.

ACKNOWLEDGMENTS

The financial support from the Defence Research and Development Organization, India, and the United States Office of Naval Research, through ONR Grant No. N00014-95-1-0132, is acknowledged. The authors are grateful to Dr. Y.R. Mahajan, Scientist "G", and Dr. D. Banerjee, Director, Defence Metallurgical Research Laboratory (Hyderabad, India), for valuable suggestions, encouragement, and support extended during the progress of this work. Gratitude is expressed to Mr. M. Srinivasa Rao, Technical Officer, for his technical assistance in hot pressing. Some of the TEM work was performed at the Materials Research Center Facilities, Northwestern University, supported by the NSF under Grant No. DMR-9632742 during the sabbatical leave of RM, and the cooperation of Dr. W.-A. Chiou, Research Associate Professor, is gratefully acknowledged.

REFERENCES

1. J.J. Petrovic: *Ceram. Eng. Sci. Proc.*, 1997, vol. 18 (3), pp. 3-17.
2. R.M. Aikin, Jr.: *Scripta Metall. Mater.*, 1992, vol. 26, pp. 1025-30.
3. D.H. Carter, J.J. Petrovic, R.E. Honell, and W.S. Gibbs: *Ceram. Sci. Eng. Proc.*, 1989, vol. 10, pp. 1121-29.
4. S.R. Srinivasan, R.B. Schwarz, and J.D. Embury: *Materials Research Society Symp. Proc.*, Materials Research Society, Pittsburgh, PA, 1993, vol. 288, pp. 1099-1104.
5. S.R. Srinivasan and R.B. Schwarz: *Novel Powder Processing, Advances in Powder Metallurgy and Particulate Materials—1992*, MPIF, Princeton, NJ, 1992, vol. 7, pp. 345-58.
6. R. Mitra, Y.R. Mahajan, N.E. Prasad, and W.-A. Chiou: *Mater. Sci. Eng. A*, 1997, vol. 225, pp. 105-17.
7. H. Chang, H. Kung, and R. Gibala: *Materials Research Society Symp. Proc.*, D.B. Miracle, D.L. Anton, and J.A. Greaves, eds., Materials Research Society, Pittsburgh, PA, 1992, vol. 273, pp. 253-58.
8. D.A. Hardwick, P.L. Martin, S.N. Patankar, and J.J. Lewandowski: in *Structural Intermetallics*, R. Darolia, J.J. Lewandowski, C.T. Liu, P.L. Martin, D.B. Miracle, and M.V. Nathal, eds., TMS, Warrendale, PA, 1993, pp. 665-74.
9. S.A. Maloy, A.H. Heuer, J.J. Lewandowski, and J.J. Petrovic: *J. Am. Ceram. Soc.*, 1991, vol. 74 (10), pp. 2704-06.
10. J.S. Jayahankar, E.N. Ross, P.D. Eason, and M.J. Kaufman: *Mater. Sci. Eng.*, 1997, vol. A239, pp. 485-92.

11. J.J. Petrovic: *Mater. Sci. Eng. A*, 1995, vols. 192-193, pp. 31-37.
12. R.M. Aikin, Jr.: *Mater. Sci. Eng. A.*, 1992, vol. 155, pp. 121-33.
13. K. Ito, H. Inui, Y. Shirai, and M. Yamaguchi: *Phil. Mag.*, 1992, vol. A72, pp. 1075-97.
14. S.A. Maloy, A.H. Heuer, J.J. Lewandowski, and T.E. Mitchell: *Acta Metall. Mater.*, 1992, vol. 40 (11), pp. 3159-65.
15. K. Ito, T. Yano, T. Nakamoto, H. Inui, and M. Yamaguchi: *Intermetallics*, 1996, vol. 4, pp. S119-S131.
16. O. Unal, J.J. Petrovic, D.H. Carter, and T.E. Mitchell: *J. Am. Ceram. Soc.*, 1990, vol. 73 (6), pp. 1752-57.
17. D.J. Evans, F.J. Scheltens, J.B. Woodhouse, and H.L. Fraser: *Phil. Mag.*, 1997, vol. 75 (1), pp. 1-15.
18. D.J. Evans, F.J. Scheltens, J.B. Woodhouse, and H.L. Fraser: *Phil. Mag.*, 1997, vol. 75 (1), pp. 17-30.
19. S.A. Maloy, T.E. Mitchell, J.J. Lewandowski, and A.H. Heuer: *Phil. Mag. Lett.*, 1993, vol. 67 (5), pp. 313-21.
20. D.J. Evans, S.A. Court, P.M. Hazzeldine, and H.L. Fraser: *Phil. Mag. Lett.*, 1993, vol. 67 (5), pp. 331-41.
21. Y. Umakoshi, T. Sakagami, T. Hirano, and T. Yamane: *Acta Metall. Mater.*, 1990, vol. 38 (6), pp. 909-15.
22. S.A. Maloy, T.E. Mitchell, and A.H. Heuer: *Acta Metall. Mater.*, 1995, vol. 43 (2), pp. 657-68.
23. U. Messerschmidt, M. Bartsch, S. Guder, D. Häuβler, R. Haushälter, and M. Yamaguchi: *Intermetallics*, 1998, vol. 6, pp. 729-33.
24. S. Guder, M. Bartsch, M. Yamaguchi, and U. Messerschmidt: *Mater. Sci. Eng.*, 1999, vol. A261, pp. 139-46.
25. K. Ito, K. Matsuda, Y. Shirai, H. Inui, and M. Yamaguchi: *Mater. Sci. Eng.*, 1999, vol. A261, pp. 99-105.
26. J.J. Petrovic, R.E. Honnell, T.E. Mitchell, R.K. Wade, and K.J. McCellan: *Ceram. Sci. Eng. Proc.*, 1991, vol. 12 (9-10), pp. 1633-42.
27. R. Gibala, H. Chang, C.M. Czarnik, K.M. Edwards, and A. Misra: in *Structural Intermetallics*, R. Darolia, J.J. Lewandowski, C.T. Liu, P.L. Martin, D.B. Miracle, and M.V. Nathal, eds., TMS, Warrendale, PA, 1993, pp. 561-67.
28. J.P. Campbell, H. Chang, and R. Gibala: *Materials Research Society Symp. Proc.*, Materials Research Society Pittsburgh, PA, 1995, vol. 364, pp. 893-98.
29. K. Sadananda, C.R. Feng, H.N. Jones, and J.J. Petrovic: in *Structural Intermetallics*, R. Darolia, J.J. Lewandowski, C.T. Liu, P.L. Martin, D.B. Miracle, and M.V. Nathal, eds., TMS, Warrendale, PA, 1993, pp. 809-18.
30. A.K. Ghosh and A. Basu: *Critical Issues in the Development of High Temperature Structural Materials*, N.S. Stoloff, D.J. Duguatte, and A.F. Gramaei, eds., TMS, Warrendale, PA, 1993.
31. K. Sadananda and C.R. Feng: *Mater. Sci. Eng. A*, 1995, vols. 192-93, pp. 862-67.
32. K. Sadananda, C.R. Feng, R. Mitra, and S.C. Deevi: *Mater. Sci. Eng. A*, 1999, vol. 261, pp. 223-38.
33. K. Tanaka, H. Onome, H. Inui, M. Yamaguchi, and M. Koiwa: *Mater. Sci. Eng. A*, 1997, vols. A239-A240, pp. 188-94.
34. J.C.M. Li: *Trans. TMS-AIME*, 1963, vol. 227, pp. 239-47.
35. H. Gleiter, E. Hornbogen, and G. Baro: *Acta Metall.*, 1968, vol. 16, pp. 1053-67.
36. C.W. Price and J.P. Hirth: *Mater. Sci. Eng. A*, 1972, vol. 9, pp. 15-18.
37. J. Weertman: *J. Appl. Phys.*, 1955, vol. 26, pp. 1213-17.
38. J.H. Hollomon: *Trans. AIME*, 1945, vol. 162, pp. 268-90.
39. P. Ludwik: *Elemente der Technologischen Mechanik*, Springer, Berlin, 1909, p. 32.
40. S.V. Ramani and P. Rodriguez: *Scripta Metall.*, 1970, vol. 4, pp. 755-60.
41. E.W. Hart: *Acta Metall.*, 1967, vol. 15, pp. 351-55.
42. J.J. Jonas, R.A. Holt, and C.E. Coleman: *Acta Metall.*, 1976, vol. 24, pp. 911-18.
43. M.F. Ashby: *Phil. Mag.*, 1970, vol. 21, pp. 399-424.
44. J.P. Hirth: *Metall. Trans.*, 1972, vol. 3, pp. 3047-67.
45. J.P. Hirth and J. Lothe: *Theory of Dislocations*, John Wiley and Sons, New York, NY, 1982, p. 639.
46. R. Schroll and P. Gumbsch: *Phys. Status Solidi*, 1998, vol. A166, pp. 475-88.
47. J. Lothe: *Acta Metall.*, 1962, vol. 10, pp. 663-70.
48. R. Mitra, K. Sadananda, and C.R. Feng: submitted to *Intermetallics*.
49. G.E. Dieter: *Mechanical Metallurgy*, 3rd International ed., McGraw-Hill Book Company, Singapore, 1986, pp. 172 and 200.
50. W.G. Johnston and J.J. Gilman: *J. Appl. Phys.*, 1959, vol. 30, pp. 129-44.
51. J.J. Gilman and W.G. Johnston: *J. Appl. Phys.*, 1960, vol. 31, pp. 687-92.
52. G.R. Kegg, C.A.P. Horton, and J.M. Silcock: *Phil. Mag.*, 1973, vol. 27, pp. 1041-55.
53. A.I. Pshenichnyuk, V.V. Astanin, and O.A. Kaibyshev: *Phil. Mag. A*, 1998, vol. 77, pp. 1093-1106.
54. R. Mitra and A. Venugopal Rao: *Trans. Ind. Ceram. Soc.*, 2001, vol. 60 (1), pp. 12-20.
55. R. Mitra, V.V. Rama Rao, and A. Venugopal Rao: *Intermetallics*, 1999, vol. 7, pp. 213-32.
56. R.E. Reedhill: *Physical Metallurgy Principles*, 2nd ed. Affiliated East-West Press Pvt. Ltd., New Delhi, India, (published with permission from Litton Educational Publishing Inc., New York, NY), 1973, p. 284.